Acta Pharmaceutica Sinica B 2023;13(6):2628–2644

Chinese Pharmaceutical Association
Institute of Materia Medica, Chinese Academy of Medical Sciences

Acta Pharmaceutica Sinica B

www.elsevier.com/locate/apsb
www.sciencedirect.com

ORIGINAL ARTICLE

Hepatic COX1 loss leads to impaired autophagic flux and exacerbates nonalcoholic steatohepatitis

Qian Yu[a,b,†], Chang Li[b,c,†], Qinghui Niu[d,†], Jigang Wang[e], Zhaodi Che[f], Ke Lei[a], He Ren[a,*], Boyi Ma[a], Yixing Ren[g], Pingping Luo[f], Zhuming Fan[b], Huan Zhang[h,i], Zhaohui Liu[c], George L. Tipoe[b,*], Jia Xiao[f,g,*]

[a]*Tumor Immunology and Cytotherapy of Medical Research Center, and Center for GI Cancer Diagnosis and Treatment, the Affiliated Hospital of Qingdao University, Qingdao 266000, China*
[b]*Bau Institute of Medical and Health Sciences Education and School of Biomedical Sciences, LKS Faculty of Medicine, the University of Hong Kong, Hong Kong 999077, China*
[c]*School of Biomedical Sciences, the Chinese University of Hong Kong, Hong Kong 999077, China*
[d]*Department of Liver Center, the Affiliated Hospital of Qingdao University, Qingdao 266000, China*
[e]*Department of Pathology, the Affiliated Hospital of Qingdao University, Qingdao 266000, China*
[f]*Clinical Medicine Research Institute and Department of Metabolic and Bariatric Surgery, the First Affiliated Hospital of Jinan University, Guangzhou 510632, China*
[g]*Department of General Surgery, and Institute of Hepato-Biliary-Pancreas and Intestinal Disease, Affiliated Hospital of North Sichuan Medical College, Nanchong 637000, China*
[h]*Department of Applied Biology and Chemical Technology, the Hong Kong Polytechnic University, Hong Kong 999077, China*
[i]*Research Center for Chinese Medicine Innovation, the Hong Kong Polytechnic University, Hong Kong 999077, China*

Received 15 November 2022; received in revised form 5 February 2023; accepted 28 February 2023

KEY WORDS

Autophagy;
Inflammation;
Lipid metabolism;
Nonalcoholic fatty liver

Abstract The mechanisms underlying autophagic defects in nonalcoholic steatohepatitis (NASH) remain largely unknown. We aimed to elucidate the roles of hepatic cyclooxygenase 1 (COX1) in autophagy and the pathogenesis of diet-induced steatohepatitis in mice. Human nonalcoholic fatty liver disease (NAFLD) liver samples were used to examine the protein expression of COX1 and the level of autophagy. *Cox1*$^{\Delta hepa}$ mice and their wildtype littermates were generated and fed with 3 different NASH models. We found that hepatic COX1 expression was increased in patients with NASH and diet–induced

*Corresponding authors.
E-mail addresses: edwinsiu@connect.hku.hk (Jia Xiao), tgeorge@hku.hk (George L. Tipoe), herenrh@163.com (He Ren).
[†]These authors made equal contributions to this work.
Peer review under the responsibility of Chinese Pharmaceutical Association and Institute of Materia Medica, Chinese Academy of Medical Sciences.

https://doi.org/10.1016/j.apsb.2023.03.008

disease;
Cyclooxygenase 1;
Phosphatidylinositol 3-phosphate;
WD repeat domain;
Phosphoinositide interacting 2;
Autophagosome maturation

NASH mice models accompanied by impaired autophagy. COX1 was required for basal autophagy in hepatocytes and liver specific COX1 deletion exacerbated steatohepatitis by inhibiting autophagy. Mechanistically, COX1 directly interacted with WD repeat domain, phosphoinositide interacting 2 (WIPI2), which was crucial for autophagosome maturation. Adeno-associated virus (AAV)-mediated rescue of WIPI2 reversed the impaired autophagic flux and improved NASH phenotypes in *Cox1*$^{\Delta hepa}$ mice, indicating that COX1 deletion-mediated steatohepatitis was partially dependent on WIPI2-mediated autophagy. In conclusion, we demonstrated a novel role of COX1 in hepatic autophagy that protected against NASH by interacting with WIPI2. Targeting the COX1−WIPI2 axis may be a novel therapeutic strategy for NASH.

1. Introduction

Nonalcoholic liver disease (NAFLD) has become the most common cause of chronic liver disease worldwide, with an estimated prevalence of 25% in the global adult population[1]. The disease evolves from simple steatosis to nonalcoholic steatohepatitis (NASH) and ultimately progresses to advanced cirrhosis[1]. NASH is considered a reversible condition in which the reduction of hepatic lipid accumulation could slow or even stop the progression to liver fibrosis[2]. Although lifestyle modification remains the cornerstone therapy for NASH, it is not always practical or sufficient[2]. Hence, there is an urgent need for pharmacological interventions against more severe forms of NASH. Consequently, different approaches have been recently explored to modulate lipid synthesis or promote lipid degradation, such as firsocostat and elafibranor[2–4].

Macroautophagy (referred to as autophagy) is an evolutionarily conserved degradative pathway that regulates excessive lipid droplets (LDs), damaged organelles, and protein aggregates into double-membrane autophagosomes for subsequent lysosomal degradation[5]. Hepatocytes maintain a relatively higher basal autophagy level due to the abundance of lysosomes to allow constitutive turnover of cytosolic components[5,6], which is crucial for hepatic and systemic energy homeostasis[7]. A mounting body of evidence has revealed that dysregulated autophagy during the development and progression of NASH significantly impairs autophagic flux, causes excessive lipid accumulation and induces local sterile immunity, leading to evident hepatic steatosis, oxidative stress, and inflammation[5]. However, deregulation mechanisms of autophagy under NASH conditions have not yet been thoroughly investigated. A better mechanistic understanding of the hepato-protective roles of autophagy in NASH and their possible links to lipid metabolism and inflammation would undoubtedly promote the development of autophagy-specific therapeutics for various metabolic diseases.

Cyclooxygenases (COXs) are key enzymes responsible for the biosynthesis of prostaglandins (PGs) from arachidonic acid[8]. COX1 is the constitutive form of the COX enzyme family, whereas COX2 is inducible by various stimuli, including cytokines, growth factors, hormones, and tumor promoters[9]. Most of the published reports focus on the role COX2 in liver diseases rather than that of COX1 because COX2 is overexpressed in most hepato-pathological conditions and because inhibitors of COX2 exhibit observable therapeutic outcomes in both human and rodent models. In our previous study, we first demonstrated that basal expression of COX1 was essential for hepatic homeostasis in chemically induced acute liver injury by using a whole-body knockout of *Cox1* mice[10]. In this study, by constructing *Cox1* hepatocyte-specific transgene mice, we identified a novel role of COX1 in protecting hepatic autophagy under metabolic stress. We found that a direct binding between COX1 and WIPI2 was essential for the maturation of autophagosomes and subsequent fusion with lysosomes, illustrating a protective role of the COX1−WIPI2 axis in the pathogenesis of NASH.

2. Materials and methods

2.1. Adeno-associated virus 8 (AAV8) vector production

A recombinant adeno-associated virus 8 (rAAV8) inverted terminal repeats-containing plasmid (pAV-CMV-P2A-GFP) with an expression cassette containing inverted terminal repeats was used for rAAV8 generation. To generate AAV8-WIPI2, we used the sequence of mouse *Wipi2* coding DNA sequence (CDS) from the National Center for Biotechnology Information (NCBI) (GenBank: NM_178398.4). CDS of *Wipi2* was then subcloned into the rAAV8 vector upstream of an in-frame DYKDDDDK (FLAG) tag and under the control of a CMV promoter. The vector also contained a green fluorescent protein (GFP) reporter downstream of the FLAG tag and was separated by a P2A self-cleaving peptide. The plasmid was confirmed by restriction enzymes and sequencing. The packaging, purification, and titration of the reassembled viral vector were carried out by Shanghai Integrated Biotech Solutions (Shanghai, China). The AAV8-GFP virus was used as a negative control.

2.2. Patient samples

Frozen liver samples were obtained from the Affiliated Hospital of Qingdao University and the First Affiliated Hospital of Jinan University, China. Frozen liver samples (from surgical resection) from 9 individuals of different ages obtained from peritumoral tissues were processed for Western blotting. Three samples had normal histology, and 6 patients had cirrhosis superimposed with NASH. Formalin-fixed, paraffin-embedded biopsy samples from 4 additional patients with normal histology and 8 patients with NASH diagnosed by ultrasonic and computed tomography results were processed for immunohistochemistry (IHC). The study protocol conformed with the ethical guidelines of the Affiliated

Hospital of Qingdao University, informed consent was obtained from all patients, and approval was obtained from the respective review boards for the protection of human subjects in research. The ethical code for the human liver sample experiments was QYFYWZLL27326. All used antibodies are listed in Supporting Information Table S1.

2.3. Animal experiments

Cox1 floxed mice ($Cox1^{f/f}$) were bought from the Jackson Laboratory (stock No. 030884). Hepatocyte-specific knockout mice for *Cox1* ($Cox1^{\Delta hepa}$) were generated by breeding $Cox1^{f/f}$ mice with *albumin-Cre* (*Alb-Cre*) C57/B6 transgenic mice. Animals were housed under specific pathogen-free conditions with 12-h light−dark cycle and *ad libitum* access to water and food in the animal facility of the University of Hong Kong.

Steatohepatitis was induced by feeding 8-week-old $Cox1^{\Delta hepa}$ mice and their $Cox1^{f/f}$ littermates with either a high-fat diet (HFD) rich in saturated fat and sucrose (TP23100, Trophic Diets, Nantong, China) for 8 weeks[11], a choline-deficient, L-amino acid-defined, high-fat diet enriched with 1% cholesterol (CDAA) (TP3622657; Trophic Diets) for up to 4 weeks[12], or a methionine- and choline-deficient diet (MCD) (TP3005; Trophic Diets) for 4 weeks[13], respectively. Food intake and body weight were measured weekly, and all animals consumed similar amounts of diet. Six to nine animals per experimental group were analyzed in our experiments. In our pilot studies, we did not find any observable sex difference in NASH phenotypes between male and female mice (data not shown). Thus, we only included male mice in subsequent animal experiments. Pharmacological modulation of autophagy was achieved with intraperitoneal administration of chloroquine (60 mg/kg) (T8689; TargetMol, MA, USA) or rapamycin (2 mg/kg) (T1537; TargetMol).

In a different cohort, 8-week-old male $Cox1^{\Delta hepa}$ mice were injected through the tail vein with either AAV8-WIPI2 or control GFP vectors (Shanghai Integrated Biotech Solutions, Shanghai, China) at 5.0×10^{11} genome copies, which was followed by a CDAA diet feeding for 4 weeks. At the end of the experiments, blood and liver samples were collected for biochemical and histological analyses, and liver to body weight ratios were assessed. All animal experiments were conducted in accordance with the regulations of the Committee on the Use of Live Animals in Teaching and Research at the University of Hong Kong (CULATR No.: 4225-17).

2.4. Immunoprecipitation

HEK293T cells (Cell Bank of Chinese Academy of Sciences, Shanghai, China) were lysed in lysis buffer (P0013, Beyotime Biotechnology, Shanghai, China) with a protease inhibitor cocktail (HY-K0010; MedChemExpress, NJ, USA) on ice for 10 min. Cell extracts were obtained by centrifugation at 15,000 rpm (Microfuge 20; Bechman Coulter Life Sciences, IN, USA) at 4 °C for 15 min to remove cell debris. The protein concentration of the cell extract was detected by bicinchoninic acid (23223; Thermo Fisher Scientific, MA, USA). Cell lysates were incubated with 2 μg FLAG antibody (PA1-984B; Thermo Fisher Scientific) or Normal Rabbit IgG (12-370; Sigma−Aldrich, Saint Louis, MO, USA) and Protein A/G Magnetic Beads (88803; Thermo Fisher Scientific) at 4 °C overnight, which was followed by separation with a magnetic stand. Beads were washed twice with wash buffer (25 mmol/L Tris-HCl, pH 7.4; 150 mmol/L sodium chloride; 1 mmol/L EDTA; 1% NP-40; and 5% glycerol) and once with ultrapure water. Bound proteins were eluted with elution buffer (0.1 mol/L glycine·HCl, pH 2.0), neutralized with a buffer (1 mol/L Tris, pH 8.5), and boiled in 4× sample buffer. Proteins were separated using 10% SDS-PAGE. Protein signals were quantified and analyzed with ImageJ software (National Institutes of Health, MD, USA).

2.5. Transmission electron microscopy

AML12 cells (Cell Bank of Chinese Academy of Sciences) or mice liver tissues were fixed in 2.5% (*v*/*v*) glutaraldehyde (G1102; Servicebio, Wuhan, China) for 2−4 h after transfection of si*Cox1* (sc-35097; Santa Cruz Biotechnology, Dallas, TX, USA) or si*Ctrl* (sc-37007; Santa Cruz Biotechnology) for 48 h. Cells/tissues were then washed with 0.1 mol/L phosphate buffer (pH 7.4) 3 times (15 min/time), which was followed by dehydration with a gradient of concentrations of alcohol and acetone for 15 min. Then, the cells were incubated in a 1:1 mixture of 100% (*v*/*v*) acetone and embedding medium for 2−4 h, which was followed by incubation in pure embedding medium for 5−8 h and maintenance at 40 °C overnight for the embedding medium to permeate the capsule. Cells/tissues were then polymerized at 60 °C for 48 h. Next, sections of the cell/tissue samples (60−80 nm) were prepared using a Leica UC7 (Wetzlar, Germany) and stained with 2% saturated acetic acid uranium and with citric acid each for 15 min. The samples were observed under transmission electron microscopy (TEM) (HT7700; Hitachi, Tokyo, Japan).

2.6. Surface plasmon resonance (SPR) and microscale thermophoresis (MST)

The analysis of the direct interactions between WIPI2 and COX1 was performed at 25 °C on a BIAcore S2100 SPR instrument (GE Healthcare, IL, USA) as previously described[14]. In brief, recombinant mouse COX1 protein (Lot No. P04012021; MerryBio, Nanjing, China) was immobilized *via* amine coupling on a flow cell of the chip. The remaining binding sites on the chips were blocked with 1 mol/L ethanolamine (pH 8.5) at a flow rate of 10 μL/min for 5 min. Recombinant mouse WIPI2 (Lot No. P30093114; MerryBio, Nanjing, China) was diluted in the running buffer and then injected at different concentrations and passed over adjacent target and control flow cells at a flow rate of 30 μL/min for 180 s, and the decomposition period was adjusted to 300 s. The bound analytes were removed with a 30 s wash in running buffer.

MST experiments were performed on a Monolith NT.115 Blue/Green Machine (NanoTemper Technologies, Munich, Germany). For binding studies of COX1 (in 1 × phosphate-buffered saline [PBS] with 0.05% Tween 20) to WIPI2 (in 1 × PBS with 0.05% Tween 20), the following proteins were used: 100 nmol/L of labeled WIPI2, with 3.5 μmol/L as the highest and 0.107 nmol/L as the lowest COX1 concentration. Protein samples were incubated for 10 min at ambient temperature, transferred into premium glass capillaries (NanoTemper Technologies), and measured at 60% MST power (25 °C). All dissociation constants (K_d) were calculated to a binding model assuming a 1:1 stoichiometric ratio per binding partner as described previously[15].

2.7. Binding model of COX1 and WIPI2

Since the crystal structure of WIPI2 was unavailable, we built its 3-dimensional 3D atomic model using Iterative Threading Assembly Refinement (I-TASSER)[16]. The first model created with I-

TASSER had the highest confidence and an estimated TM-score[17] equaling 0.63 ± 0.14 and was selected as the potential WIPI2 model. The crystal structure of the human COX1 (PDB code: 6Y3C) was derived from Protein Data Bank. To probe the binding mode between COX1 and WIPI2, a protein−protein docking study was carried out. Then, a set of 100 alternative models were produced using the docking method HDOCK with default settings[18]. The best-scored model generated by HDOCK was prepared using the tLEaP module in Amber16[19], and the force field parameters of the ff14SB[20] force field were assigned to the proteins. The model was then minimized in vacuo by 2000 cycles of the steepest descent and 3000 cycles of conjugate gradient minimizations. Finally, the binding free energy was calculated using molecular mechanics with generalized Born and surface area solvation (MM/GBSA)[21] with the modified GB (GBOBC1) model[22]. The interior (solute) and exterior dielectric constants were set to 1 and 80, respectively.

2.8. Molecular dynamics (MD) simulations

Protein structures of COX1−WIPI2 complex and free WIPI2 were prepared by the advanced PDB-Preparation tool in Yinfo Cloud Computing Platform using PDBFixer and the tLEaP module in AmberTools 20. MD simulations were performed using AmberTools 20 package with AMBER ff19SB force field[23]. The system was solvated by a truncated octahedron water box using OPC water model with a margin of 10 Å. Periodic boundary condition was applied, and the net charge was neutralized by Na^+ counterions. Nonbonded van der Waals interactions were calculated using the Lennard-Jones 12-6 potentials with a 10 Å cutoff, while long-range electrostatics were treated using the Particle Mesh Ewald algorithm[24]. The SHAKE algorithm was applied to constrain bonds involving hydrogen atoms[25]. To remove improper atom contacts, the structure was first minimized by 1) 2500 steps of steepest descent and 2500 steps of conjugate gradient under a harmonic constraint of 10.0 kcal/(mol·Å^2) on heavy atoms, 2) 10,000 steps of steepest descent and 10,000 steps of conjugate gradient with a constraint on only protein backbone, and 3) relaxing the entire system by 10,000 steps of steepest descent and 10,000 steps of conjugate gradient. The system was gradually heated up to 300 K by a 20 ps NVT simulation. Next, two steps of equilibration phases were carried out: 1) a 200 ps NPT simulation with constraints on heavy atoms; 2) a 500 ps NVT simulation without restraint. The temperature was maintained at 300 K using the Berendsen thermostat with 1 ps coupling constant and the pressure at 1 atm using Monte Carlo barostat with 1 ps relaxation time. Finally, each system was subjected to a 100 ns NVT simulation with a time step of 2 fs. The root-mean-square deviation, root-mean-square fluctuation, radius of gyration, and distance measurement were analyzed by the CPPTRAJ module[26], while principal component analysis and cross-correlation analysis were analyzed by R package Bio3D[27]. At last, PyMOL software (Version 2.5) was employed to visualize binding modes of COX1 and WIPI2, and Visual Molecular Dynamics[28] was applied to make movies of MD trajectories.

2.9. Statistical analysis

The Prism 8 software (GraphPad Software, CA, USA) containing SPSS 21.0 (IBM Corp, NY, USA) was used for statistical analysis in our study. The differences analyses were evaluated using a one-way analysis of variance (ANOVA) followed by Tukey *post hoc* test or the Student's *t* test (followed by a Mann−Whitney test) to detect statistical differences between groups. The correlation analyses were calculated with Pearson correlation coefficients. A *P* value below 0.05 was considered statistically significant.

Additional materials and methods are included in the Supporting Information.

3. Results

3.1. COX1 expression increased in NASH patients and diet-induced NASH mice models accompanied by impaired autophagy

Existing research is yet to characterize expressional changes of COX1 during steatohepatitis progression. We searched the Gene Expression Omnibus database (GSE130970 and GSE126848) for *Cox1* gene expressions and found that *Cox1* mRNA levels were significantly increased in patients with NASH compared to healthy controls (Fig. 1A). A statistically significant positive correlation was detected between mRNA levels of *Cox1* and *Lc3b*, indicating a close association between *Cox1* and autophagy (Fig. 1B). We then validated these findings and found increased expression of COX1 in the livers of NASH patients compared to controls as determined by IHC (Fig. 1C). To further assess the relevance between COX1 expression and autophagic activity, we tested liver samples from NASH patients, CDAA-induced, and HFHC diet-induced NASH mice models and found significant increases in LC3II, p62, and COX1 protein levels compared to their control samples (Fig. 1D−F). These results indicate that increased COX1 expressions in the livers of NASH patients and diet-induced murine NASH models might be associated with impaired autophagic flux.

3.2. COX1 was required for basal autophagy in hepatocytes

To further examine the physiological role of *Cox1* in hepatocytes, we employed RNAi-mediated depletion of *Cox1* in the murine normal hepatocyte line AML12 cells. Interestingly, a substantial accumulation of large translucent vacuoles in *Cox1*-knockdown cells was observed under light microscopy (Fig. 2A). This phenotype possibly resulted from disrupted autophagic flux, as reported by previous studies[29,30]. In addition, these vacuoles appeared to be enriched with the lysosomal membrane protein lysosome-associated membrane protein 1 (LAMP1) (Fig. 2B), indicating that the large-sized vacuoles might be partially derived from lysosomes. Further, the "circles" were also partially positive for LC3, indicating autophagic vacuoles (Supporting Information Fig. S1). Under electron microscopy, ablation of COX1 induced an accumulation of large autophagic bodies within the vacuoles (Fig. 2C), which was in line with an accumulation of the autophagic markers, LC3II and p62 (Fig. 2D). These results suggest that disruption of COX1 could impair basal autophagic flux in hepatocytes.

3.3. Autophagy flux is blocked in Cox1-knockdown AML12 cells

The entire autophagic process can be generally divided into 1) formation of autophagosomes, 2) autophagosome maturation and fusion with lysosomes, and 3) degradation within lysosomes[31,32]. The accumulation of the autophagosome marker LC3II in the knockdown conditions could result from 1) increased autophagy onset, 2) impaired autophagosome maturation, or 3) defective lysosomal degradation. To address this, we first analyzed autophagosome maturation/autophagosome−lysosome fusion using a Tandem RFP-GFP-LC3 sensor based on the pH difference

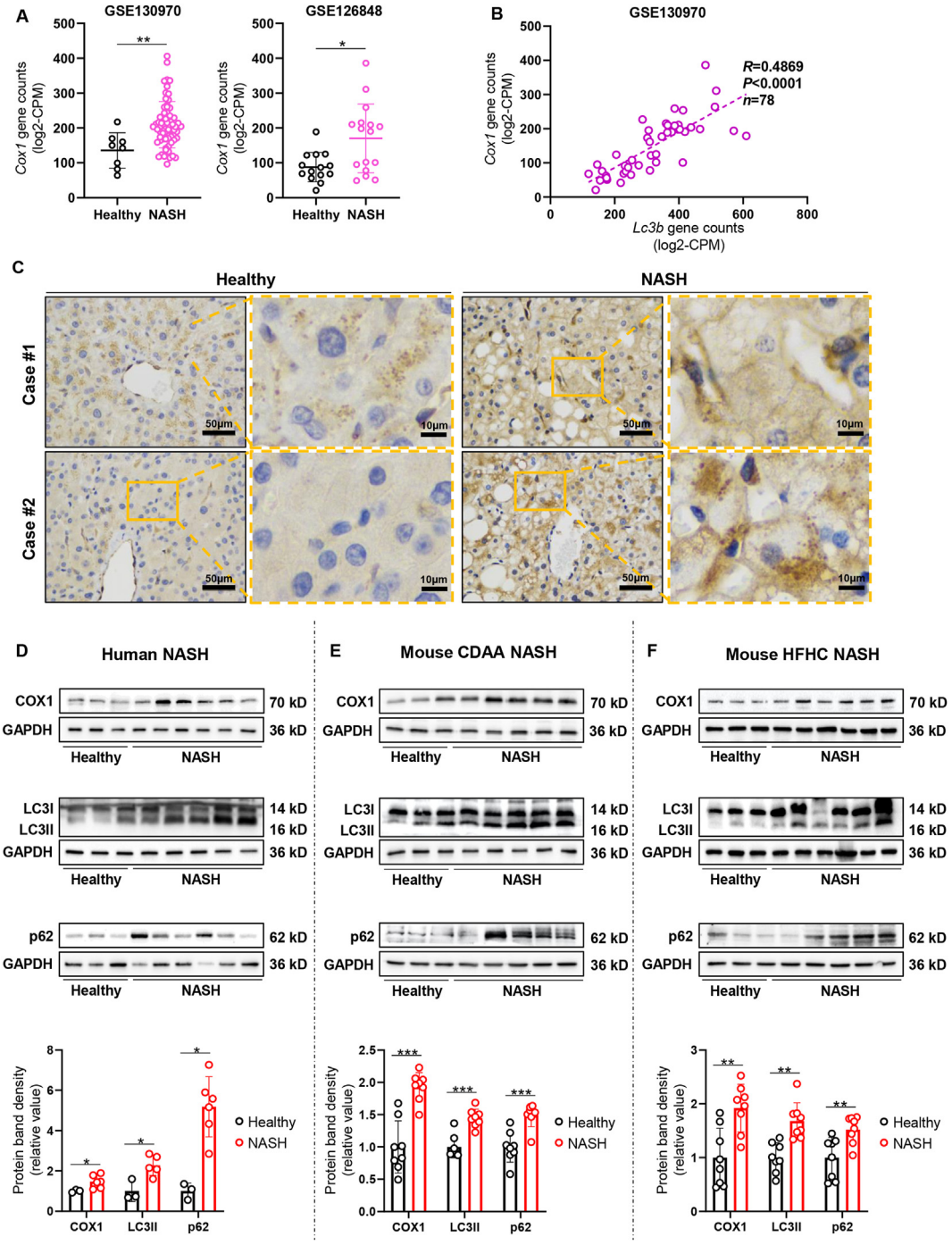

Figure 1 NASH in the mice model and human samples was associated with increased COX1 expression and impaired autophagic flux. (A) Comparison of the expression of *Cox1* mRNA between healthy controls and patients with NASH in the GEO database (GSE130970 and GSE126848). (B) The correlation between *Cox1* with *Lc3b* in control and NASH specimens from the GEO database (GSE130970) was analyzed ($n = 78$), and the linear regression coefficient and statistical significance are indicated. The gene level counts of *Cox1* and *Lc3b* were normalized to log2-counts per million reads (CPM). (C) The protein expression of COX1 was detected using IHC staining in liver tissues of the representative controls ($n = 4$) and NASH patients ($n = 8$). Scale bar = 50 μm. Protein levels and Western blotting analysis for COX1, LC3I/II, and p62 from livers of the controls ($n = 3$) and patients with NASH ($n = 6$) (D), from livers of normal diet and CDAA diet−fed mice ($n = 8$/group) (E), and from livers of normal diet and HFHC diet-induced NASH mice models ($n = 8$−9/group) (F). GAPDH was used as a loading control. Values represent means ± SD. Statistical comparisons between groups were analyzed using the Student's *t* test. $^{*}P < 0.05$; $^{**}P < 0.01$; $^{***}P < 0.001$. NASH, nonalcoholic steatohepatitis; CDAA, a choline-deficient, L-amino acid-defined, high-fat diet enriched with 1% cholesterol; HFHC, a high-fat diet rich in saturated fat and sucrose; CPM, counts per million reads.

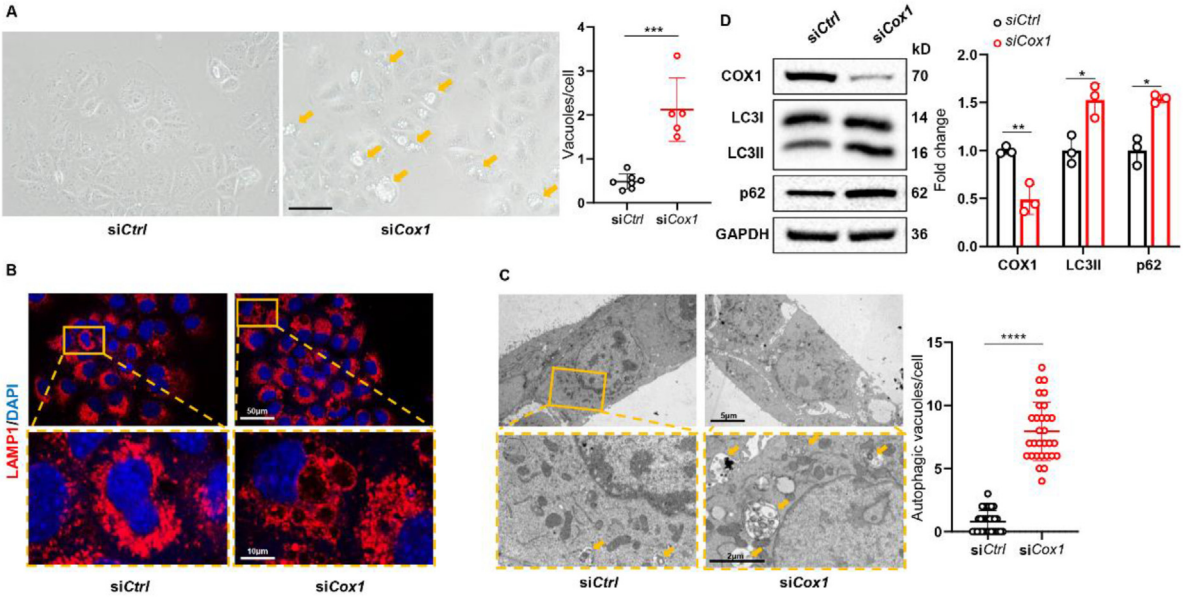

Figure 2 COX1 was required for basal autophagy *in vitro*. (A) Large translucent vacuoles (orange arrowheads) were observed and quantified in the *Cox1*-knockdown AML12 cells using brightfield microscopes ($n = 5-10$ fields, which contains 400−600 cells in each group). Scale bar = 100 μm. (B) Representative confocal images of LAMP1 indicated enlarged vacuoles in si*Ctrl* and si*Cox1* AML12 cells. Scale bar = 50 μm (original) and 10 μm (zoom-out part). (C) *Cox1*-knockdown induced the accumulation of autophagic vacuoles as shown in the electron micrographs, which were quantified on the right side ($n = 30$ cells/group). Orange arrowheads indicate typical autophagosomes/autolysosomes. Scale bar = 5 μm (original) and 2 μm (zoom-out part). (D) Representative Western blotting images of COX1, LC3I/II, and p62 in si*Ctrl* and si*Cox1* AML12 cells. Values represent means ± SD. Statistical comparisons between groups were analyzed using the Student's *t* test. ***$P < 0.001$, ****$P < 0.0001$. Ctrl, control; LAMP1, lysosomal membrane protein lysosome-associated membrane protein 1.

between the acidic autolysosome and the neutral autophagosome. The neutral LC3-positive autophagosomes were tagged with GFP and RFP signals, therefore appearing as yellow puncta, whereas the acidic autolysosomes were exclusively shown by RFP since the acidic pH inhibited GFP signals. As shown in Fig. 3A, in si*Ctrl* cells, both red and yellow puncta were present, whereas in *Cox1*-knockdown cells, most of the LC3 puncta were yellow, indicating defective autophagosome maturation. In line with these data, GFP-LC3 puncta were markedly increased in *Cox1*-knockdown cells, which did not colocalize with LAMP1 (Fig. 3B). We then pretreated AML12 cells with bafilomycin A1 (BafA) for 6 h or chloroquine (CQ) for 4 h to impair lysosome activity, allowing us to assess autophagosome formation which was indicated by LC3II levels. Knockdown of *Cox1* failed to cause a further accumulation of LC3II upon late-stage autophagy inhibition with BafA or CQ, suggesting that *Cox1* deficiency-induced the accumulation of LC3II was not a result of increased autophagy onset (Fig. 3C). In addition, by using various autophagy inducers, including starvation, torin-1 and rapamycin—the latter of which induced autophagy *via* the suppression of mTOR/S6 kinase signaling—we further demonstrated that knocking down *Cox1* did not inhibit autophagy induction but might have disrupted autophagosome maturation (Fig. 3D−F). We also employed CRISPR/Cas9-mediated *Cox1* gene knockout in AML12 cells, with the results being consistent with those of *Cox1* knockdown under CQ treatment (Supporting Information Fig. S2). Taken together, these data demonstrate that the deletion of COX1 impaired autophagosome maturation, thus blocking the autophagosome−lysosome fusion process and contributing to the accumulation of LC3-positive autophagosomes.

3.4. *Liver-specific Cox1 deletion exacerbates steatohepatitis*

To study the effects of hepatic *Cox1* deletion *in vivo*, we bred $Cox1^{f/f}$ animals with *Alb-Cre* mice, in which the expression of *Cre* is under the control of the *albumin* promoter, allowing deletion of floxed genes specifically in the liver ($Cox1^{\Delta hepa}$) (Supporting Information Fig. S3A). $Cox1^{\Delta hepa}$ mice did not exhibit any histological differences under chow diet−fed conditions (Fig. 4A). Nevertheless, while we fed $Cox1^{\Delta hepa}$ mice and their control littermates ($Cox1^{f/f}$) with 3 different NASH model diets, including an HFHC diet for 8 weeks, an MCD diet for 4 weeks, and a CDAA diet for 4 weeks, histological staining assays demonstrated that hepatocyte-specific COX1 depletion exacerbated HFHC, MCD and CDAA diet-induced liver injury as evidenced by increased macro- and microvesicular steatosis, increased number and size of lipid droplets, and fibrosis when compared with $Cox1^{f/f}$ mice (Fig. 4A and B; Supporting Information Figs. S3B, S3C, S4A). Macroscopic analysis of livers indicated a significant increase in size in $Cox1^{\Delta hepa}$ mice after 4 weeks of CDAA treatment or 8 weeks of HFHC diet (Fig. 4C; Fig. S3D). Consistently, $Cox1^{\Delta hepa}$ mice displayed a significantly increased liver weight or the liver to body weight ratio after a 4-week CDAA diet treatment or an 8-week HFHC diet (Fig. 4C; Fig. S3E and S3F). In parallel, $Cox1^{\Delta hepa}$ mice exhibited a marked increase in hepatic triglyceride (TG) content (Fig. 4D; Fig. S3G) and significant elevations of liver injury markers (serum alanine transaminase [ALT] and aspartate transaminase [AST]) in 3 diet−induced NASH models (Fig. 4E; Fig. S3H and S3I; Fig. S4B and S4C). In the livers of $Cox1^{\Delta hepa}$ mice, we observed increased gene expressions of steatosis markers, including stearoyl-coA desaturase-1(*Scd1*), peroxisome proliferator-activated receptor

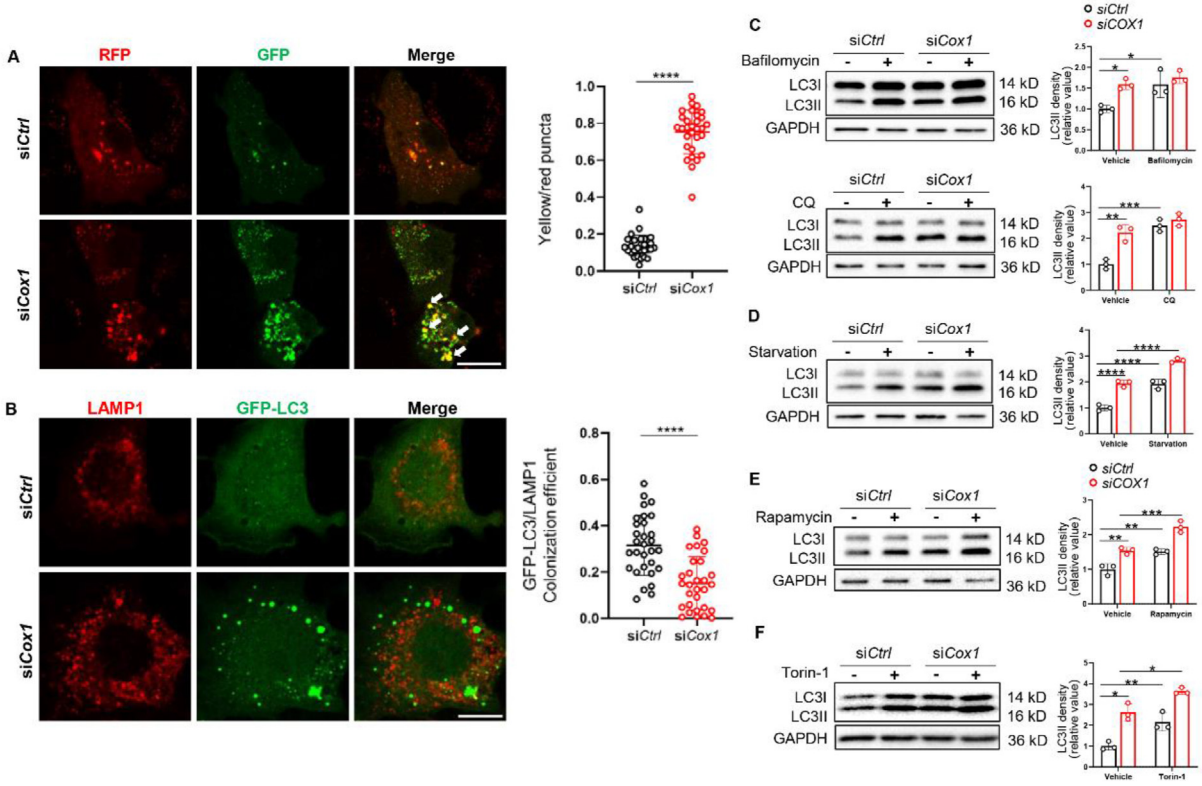

Figure 3 Autophagy flux was blocked in *Cox1*-knockdown AML12 cells. (A) Representative confocal images and quantification of LC3 yellow puncta (white arrowheads)/red puncta ($n = 30$ cells of 3 independent experiments) of tandem RFP-GFP-LC3 sensor indicating accumulation of LC3II puncta in si*Ctrl* and si*Cox1* AML12 cells. Scale bar = 10 μm. (B) Representative confocal images of the colocalization of GFP-LC3 puncta and LAMP1 in si*Ctrl* and si*Cox1* AML12 cells. Scale bar = 10 μm. The GFP-LC3 and LAMP1 colocalization coefficient is shown on the right ($n = 30$ cells of 3 independent experiments). (C) Protein expression of LC3I/II after BafA treatment (10 nmol/L) for 6 h or CQ treatment (100 μmol/L) for 4 h in si*Ctrl* and si*Cox1* AML12 cells. (D) Protein expression of LC3I/II after starvation (serum-free) for 6 h in si*Ctrl* and si*Cox1* AML12 cells. (E, F) Protein expression of LC3I/II after rapamycin (1 μmol/L) or torin-1 (1 μmol/L) treatment for 6 h in si*Ctrl* and si*Cox1* AML12 cells. The immunoblots shown are representative of the results obtained from 3 independent assays. Values represent means ± SD. Statistical comparisons between groups were analyzed using a one-way ANOVA or the Student's *t* test. $^{*}P < 0.05$; $^{**}P < 0.01$; $^{***}P < 0.001$; $^{****}P < 0.0001$. LAMP1, lysosomal membrane protein lysosome-associated membrane protein 1; CQ, chloroquine.

gamma (*Ppar-γ*) and *Cd36*, and inflammatory markers, including necrosis factor α (*Tnf-α*), interleukin 6 (*Il-6*) and interleukin 1β (*Il-1β*). These results are in line with more significant macrophage infiltration, as revealed by the IHC detection of F4/80 (Fig. 4H). These data indicate conclusively that hepatocyte-specific COX1 deficiency worsened NASH-related hepatic damage, steatosis, and inflammation.

3.5. *Hepatic COX1 deletion aggravated NASH through inhibition of autophagy*

To examine the effects of hepatic *Cox1* deletion on autophagy *in vivo*, we applied TEM on mice liver samples. We observed a significantly increased number of autophagic vacuoles in $Cox1^{\Delta hepa}$ mice compared to their control littermates, when fed with the normal diet (Fig. 5A). The CDAA diet induced large autophagic bodies and accumulated LDs in the livers of both $Cox1^{f/f}$ mice and $Cox1^{\Delta hepa}$ mice (Fig. 5A). We further analyzed the levels of the LC3I/II and autophagy substrate p62 to identify if the diet−induced autophagy or impaired autophagosome maturation in $Cox1^{\Delta hepa}$ mouse livers. Consistent with our *in vitro* data, hepatocyte-specific COX1 deficiency led to increased levels of LC3II and p62, suggesting a defective maturation of autophagosome that inhibited subsequent autophagosome−lysosome fusion (Fig. 5B and C). For $Cox1^{f/f}$ control mice, CDAA treatment increased hepatic autophagy levels as one of the key degradative pathways for excessive LDs. However, the level of LC3II was high in the liver of $Cox1^{\Delta hepa}$ mice at the basal state and was not further increased upon CDAA diet treatment, suggesting that the impaired autophagosome maturation process caused by COX1 deficiency might be the reason for the aggravated steatohepatitis (Fig. 5B and C)[29].

Since our data suggest that hepatic COX1 deletion disrupts autophagy and accelerates steatohepatitis, we further explored whether COX1 deletion contributed to diet-induced liver injury through autophagic inhibition *in vitro* and *in vivo*. In AML12 cells, COX1 deletion resulted in increased intracellular lipids as indicated by BODIPY (D3922; ThermoFisher Inc., CA, USA), while CQ treatment abrogated these effects, indicating COX1 deletion promoted lipid accumulation through inhibition of autophagy (Supporting Information Fig. S5). Furthermore, according to Lin et al.[2], suppression of autophagy with the administration of CQ 16 h before euthanizing the mice can exacerbate hepatic steatosis and liver injury with only slightly increased liver inflammation in

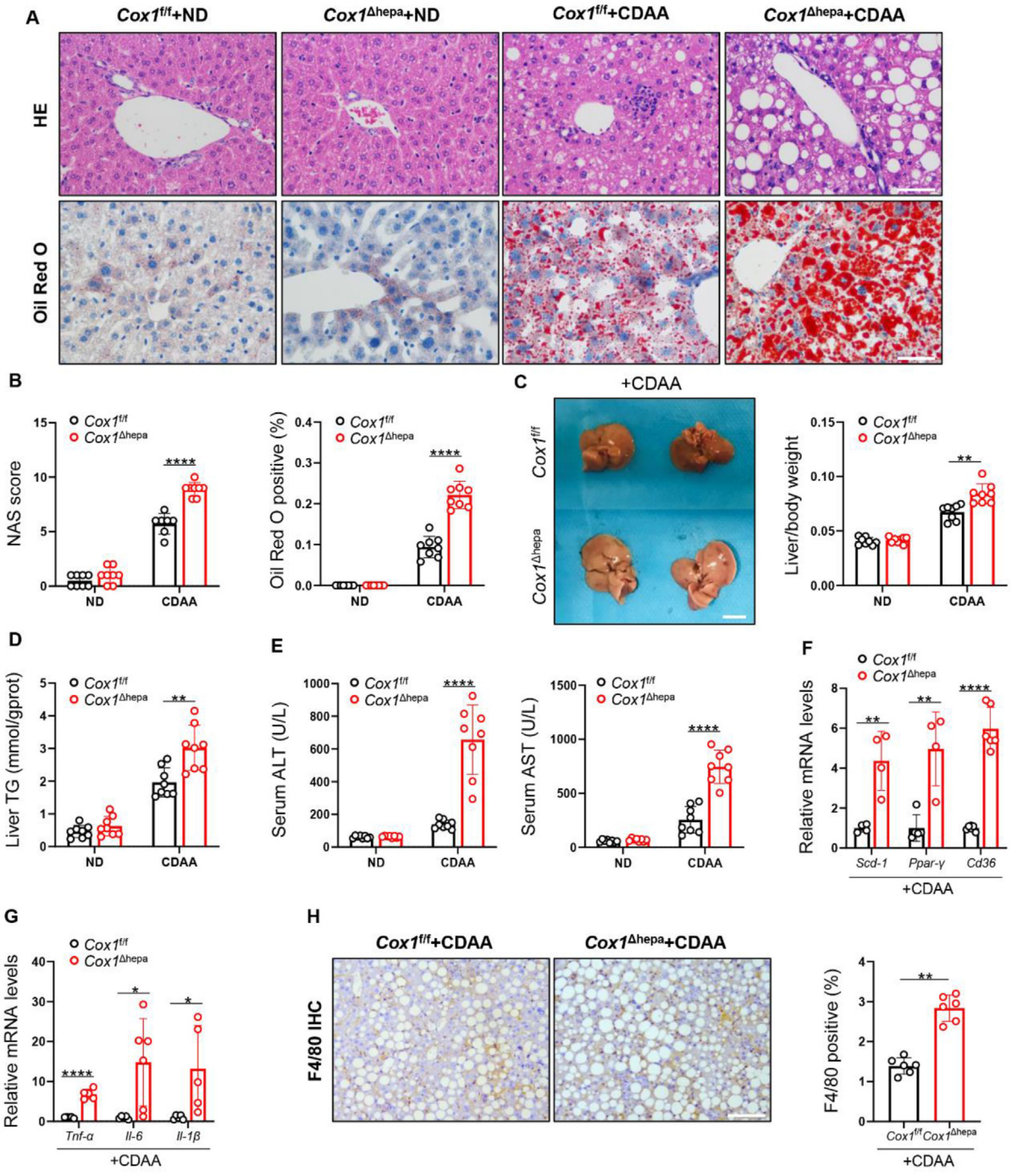

Figure 4 Hepatocyte-specific knockout of *Cox1* exacerbated steatohepatitis in the CDAA-induced mouse model. *Cox1* $^{f/f}$ and *Cox1*$^{\Delta hepa}$ mice were fed with a normal diet or a CDAA diet for 4 weeks (n = 8−9/group). (A) Representative images of livers from *Cox1*$^{f/f}$ and *Cox1*$^{\Delta hepa}$ mice on a CDAA diet for 4 weeks, stained by hematoxylin and eosin (HE) or Oil Red O. Scale bar = 50 μm. (B) The quantification of NAFLD activity score (NAS) and Oil Red O-positive area (percentage per field) of mice. (C) Representative gross anatomy of mice liver and the liver to body weight ratio. Scale bar = 1 cm. (D) Quantification of liver TG levels of mice. (E) Serum ALT and AST levels of mice. (F) mRNA levels of key genes (*Scd-1*, *Ppar-γ*, and *Cd36*) of lipid metabolism in the livers from *Cox1*$^{f/f}$ and *Cox1*$^{\Delta hepa}$ mice on a CDAA diet for 4 weeks (n = 4−6/group). (G) mRNA levels of key genes (*Tnf-α*, *Il-6*, and *Il-1β*) of inflammation in the livers from *Cox1*$^{f/f}$ and *Cox1*$^{\Delta hepa}$ mice on a CDAA diet for 4 weeks (n = 4−6/group). (H) Representative images of F4/80 IHC staining in liver sections of *Cox1*$^{f/f}$ and *Cox1*$^{\Delta hepa}$ mice on a CDAA diet for 4 weeks (n = 6/group). The percentage of F4/80-positive area per field was determined from 3 fields per section. Scale bar = 50 μm. Values represent means ± SD. Statistical comparisons among groups were analyzed using a one-way ANOVA or the Student's t test. *P < 0.05; **P < 0.01; ****P < 0.0001. HE, hematoxylin and eosin; CDAA, a choline-deficient, L-amino acid-defined, high-fat diet enriched with 1% cholesterol; ALT, alanine transaminase; AST, aspartate transaminase; TG, triglyceride; NAS, NAFLD activity score; Scd1, stearoyl-coA desaturase-1; Ppar-γ, peroxisome proliferator-activated receptor gamma; Tnf-α, necrosis factor α; Il-6, interleukin 6; Il-1β, interleukin 1β.

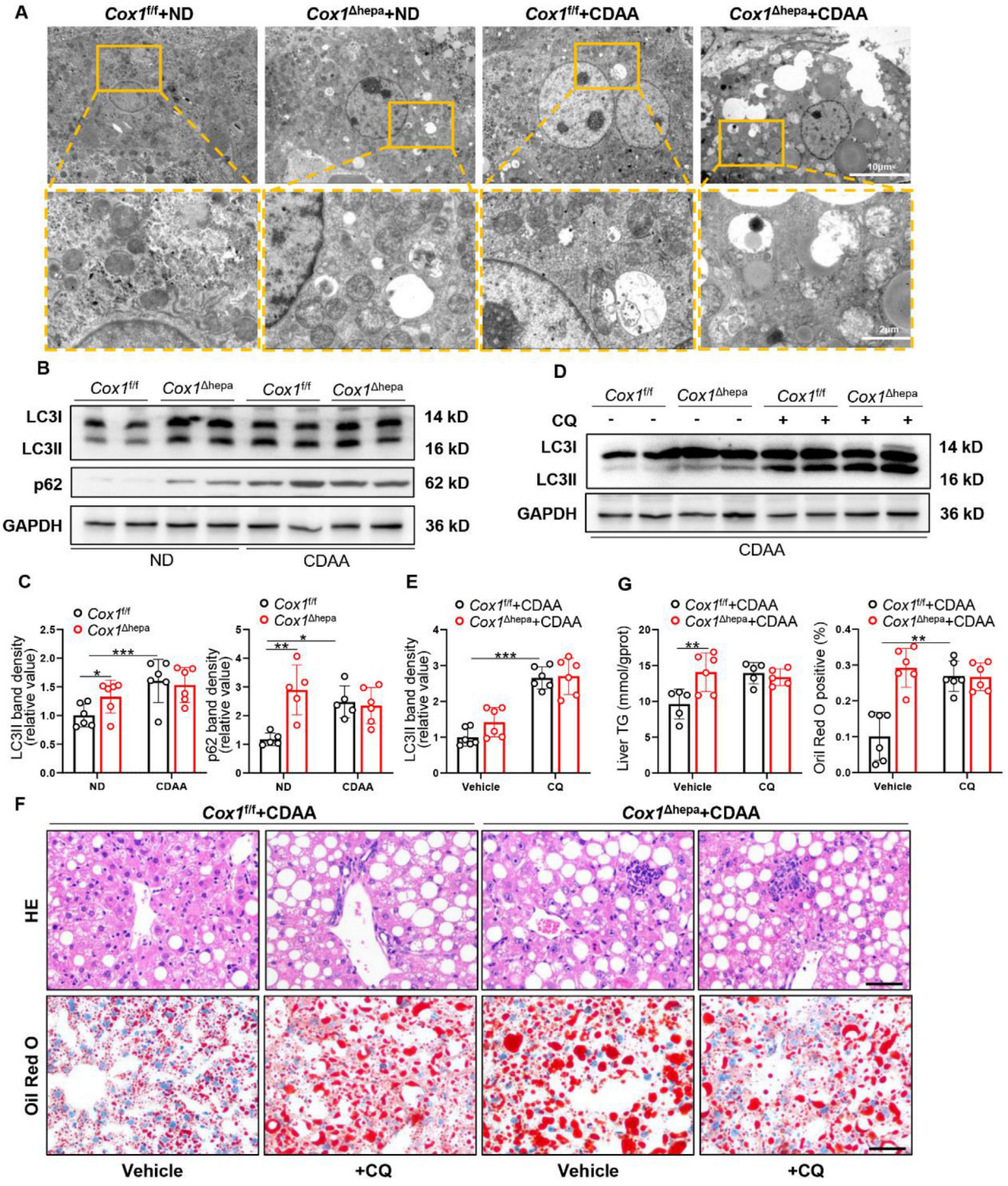

Figure 5 Inhibition of autophagy by CQ increased hepatic lipid accumulation in *Cox1*$^{f/f}$ but not in *Cox1*$^{\Delta hepa}$ mice. (A) Representative electron microscopy images of liver sections from *Cox1*$^{f/f}$ and *Cox1*$^{\Delta hepa}$ mice fed with a ND or a CDAA diet for 4 weeks. Scale bar = 10 μm (original) and 2 μm (zoom-out part). (B, C) Hepatic expression of autophagic markers LC3I/II and p62 protein levels from *Cox1*$^{f/f}$ and *Cox1*$^{\Delta hepa}$ mice fed with a ND or a CDAA diet for 4 weeks (n = 5−6/group). GAPDH was used as a loading control. (D, E) *Cox1*$^{f/f}$ and *Cox1*$^{\Delta hepa}$ mice were fed a CDAA diet for 4 weeks, which was followed by administration of NaCl or CQ 16 h before mice were sacrificed (n = 5−6/group). Hepatic expression of autophagic marker LC3I/II protein was analyzed by Western blotting. (F) Representative microscopic images of liver sections stained with HE and Oil Red O in CDAA-fed mice with NaCl or CQ administration (n = 5−6/group). Scale bar = 50 μm. (G) Hepatic TG levels and the percentage of Oil Red O-positive area per field in CDAA-fed mice with NaCl or CQ co-administration (n = 5−6/group). Values represent means ± SD. Statistical comparisons among groups were analyzed using a one-way ANOVA. *P < 0.05; **P < 0.01; ***P < 0.001. HE, hematoxylin and eosin; CDAA, a choline-deficient, L-amino acid-defined, high-fat diet enriched with 1% cholesterol; ND, normal diet; CQ, chloroquine; TG, triglyceride.

both alcoholic and non-alcoholic fatty liver conditions. In our study, we observed similar phenotypes in which pharmacological inhibition of autophagy by CQ inhibited autophagic influx with an accumulation of LC3II protein levels in the liver lysates from *Cox1*$^{f/f}$ mice, whereas these effects were compromised in *Cox1*$^{\Delta hepa}$ mice (Fig. 5D and E). CQ also exacerbated hepatic steatosis as measured by the increase in the number of LDs, the hepatic TG content, and the mRNA levels of steatosis markers, with minimal effects on inflammation (Fig. 5F and G; Supporting Information Fig. S6A and S6B). These effects were diminished in *Cox1*$^{\Delta hepa}$ mice. Given that the inhibition of autophagy abrogated the effects of hepatic COX1 deletion on steatosis and liver injury, we next investigated whether the induction of autophagy by rapamycin could restore the autophagic inhibition in *Cox1*$^{\Delta hepa}$ mice[2]. We found that rapamycin administration could reverse CDAA-induced liver injuries in control *Cox1*$^{f/f}$ mice, while the protective role of rapamycin was weakened by hepatocyte-specific COX1 deletion (Fig. S6C−S6F). Taken together, these results suggest that COX1 deletion exacerbated steatosis and liver injury by inhibiting autophagy.

3.6. *COX1 directly interacted with WIPI2*

Given that COX1 deletion impaired autophagosome maturation and blocked the autophagosome−lysosome fusion in hepatocytes *in vitro* and *in vivo*, we next sought to decipher the underlying mechanisms. Phosphatidylinositol 3-phosphate (PI(3)P) plays an essential role in autophagosome formation and autophagosome maturation[33]. It does so by recruiting the effector proteins associated with autophagy initiation that contain PI(3)P recognition motifs, such as the FYVE domain (found in DFCP1 autophagy-related protein) and the PROPPIN (β-propellers that bind phosphoinositides) repeats (found in WIPI proteins)[34,35]. To observe PI(3)P generation, we constructed 3 plasmids that expressed GFP-tagged PI(3)P binding domain FYVE (GFP-2xFYVE), mCherry-tagged DFCP1 (double FYVE domain-containing protein 1), and DsRed-tagged WIPI2. To further examine the mechanisms related to the involvement of COX1 in the autophagosome maturation process, we examined the colocalization of COX1 with these PI(3)P effector proteins. Interestingly, we found that COX1 puncta colocalized well with WIPI2 but not with GFP-tagged FYVE or mCherry-tagged DFCP1 in AML12 cells (Fig. 6A; Supporting Information Fig. S7A and S7B). Furthermore, COX1 colocalized with WIPI2 in human liver tissues under normal or NASH conditions (Fig. 6B). To examine the effects of WIPI2 deletion on autophagic flux, we used RNAi-mediated depletion of *Wipi2* in AML12 cells. Consistent with *Cox1* knockdown, knockdown of *Wipi2* failed to cause a further accumulation of LC3II upon the inhibition of late-stage autophagy with BafA or CQ, suggesting that WIPI2 deficiency-induced accumulation of LC3II may not result from increased autophagy onset but rather from impaired autophagosome maturation (Fig. S7C). To model the docking of COX1 to WIPI2, RosettaDock was used to identify low-energy conformations of protein−protein interactions. The predicted binding mode between COX1 and WIPI2 is shown in Fig. 6C. The docking results revealed that WIPI2 interacted with COX1 with the binding free energy of −58.42 kcal/mol. As shown by per-residue energy decomposition analysis (Supporting Information Table S2), WIPI2 residues Glu380, Cys248, Val249, Val41, Trp43, Val61, Gln372, Leu120, Pro204, and Lys246, along with COX1 residues Leu78, Leu92, Phe88, Lys485, Phe99, Trp98, Phe102, Arg79, Leu82, and Phe107, were the most critical residues for the complex formation. In addition, Glu380 (WIPI2) was observed to form a hydrogen bond with Lys485 (COX1). Further, we explored the effect on WIPI2 protein after binding with COX1, with these special binding sites in Fig. 6C. We performed 100 ns MD simulations for COX1−WIPI2 complex, with free WIPI2 as a control. We found that WIPI2 was extremely flexible and kinetic at large while dramatically becoming more rigid and stable when bound to COX1 (Supporting Information Fig. S8A and S8B). It became more compact after binding as shown by radius of gyration curves (Fig. S8C). Further analysis, *i.e.*, Principal Component Analysis and Cross-Correlation Analysis, revealed the changes in motion direction and patterns and residue correlations: both the motion amplitude and residue correlations of bound WIPI2 decreased, and the patterns became fuzzy and messy (Fig. S8D and S8E). Three crucial conformational changes were observed by visual comparison of MD trajectory snapshots (Fig. S8E) and by detections of residue pairs (Fig. S8F). Four main sites contributed to the conformational changes were identified, with interactions between COX1 and WIPI2 residues shown in Fig. S8G. Specifically, in site 1, a salt-bridge interaction between Glu492 (COX1) and Lys371 (WIPI2) was observed as an immediate consequence of the aforementioned movement. In site 2, hydrogen bonds between COX1 (Trp77, Asn80, Leu82, and Ser91) and WIPI2 residues (GLy224, Gly244, and Lys246) as well as another salt-bridge between Arg79 (COX1) and Asp202 (WIPI2) were detected. In site 3, hydrogen bonds formed between COX1 (Arg114 and Gly368) and WIPI2 residues (Ser178 and Thr180). Site 4 resides in the opposite face to site 1−3, where three modes of interactions were observed, including 1) hydrogen bonds between Ala12 (COX1) and His95 (WIPI2), 2) pi-cation interactions between Arg32 (COX1) and His95 and Phe99 (WIPI2), and 3) a pi−pi stacking between Trp43 (COX1) and Phe102 (WIPI2). Notably, a "sandwich" structure was observed in this site, which was expected to play a key role in maintenance of the binding state.

A specific interaction between COX1 and WIPI2 was further verified *via* exogenous co-immunoprecipitation (IP) assays (Fig. 6D and E) and endogenous IP assays (Fig. 6F) in HEK293T cells. Moreover, we applied biophysical assays, including SPR and MST, as validation tools for direct interactions[36,37]. The SPR assay revealed that COX1 directly bound to WIPI2, with a K_d of 2.89×10^{-6} mol/L (Fig. 6G), and the MST assay further demonstrated the interaction between the protein structures of COX1 and WIPI2, with a K_d of 3.95×10^{-8} mol/L (Fig. 6H). Overall, our results suggest COX1 directly interacted with the PI(3)P effector protein, WIPI2, which might facilitate the maturation of autophagosomes in hepatocytes.

3.7. *Hepatic restoration of WIPI2 reduced hepatic lipid accumulation and inflammation in Cox1*$^{\Delta hepa}$ *mice*

The interaction between COX1 and WIPI2 prompted us to investigate whether COX1 deletion-mediated effects were dependent on WIPI2-mediated autophagy. To address this possibility, *Cox1*$^{\Delta hepa}$ and *Cox1*$^{f/f}$ mice were fed with a CDAA diet for 4 weeks after the injection of the AAV8-GFP or AAV8-WIPI2 virus to achieve hepatic restoration of WIPI2 (Supporting Information Fig. S9A). As expected, AAV-mediated rescue of WIPI2 partially rescued the impaired autophagic flux, with decreasing levels of LC3II and p62 in the livers of *Cox1*$^{\Delta hepa}$ mice (Fig. 7A). In parallel, steatosis was partially improved in *Cox1*$^{\Delta hepa}$ mice but not in *Cox1*$^{f/f}$ mice after AAV8-WIPI2 virus injection as measured by hepatic TG levels, Oil Red O staining, and mRNA levels of

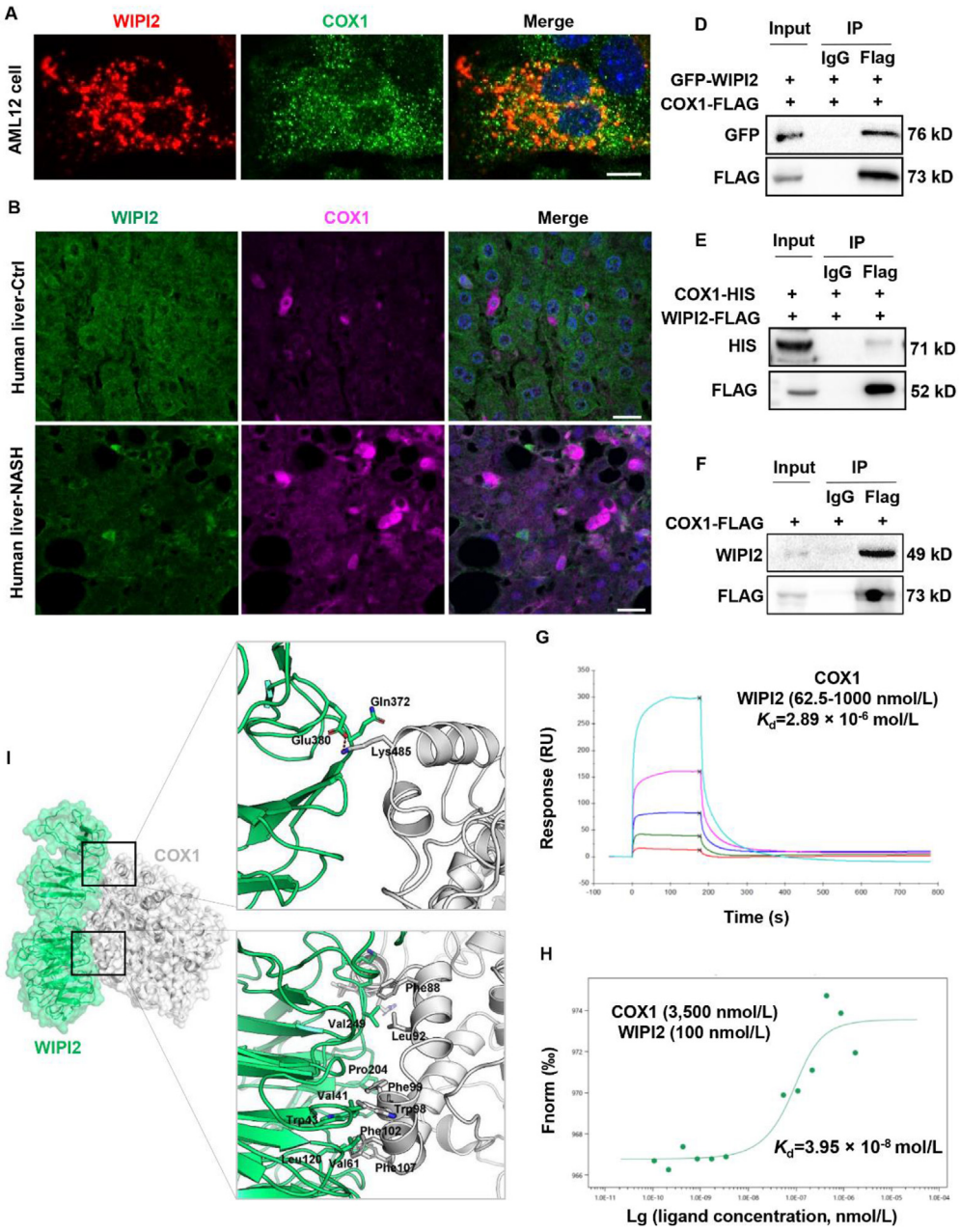

Figure 6 Direct interaction of COX1 with WIPI2. (A) Representative microscopy images of the colocalization of DsRed-WIPI2 and COX1 in AML12 cells. Scale bar = 10 μm. (B) Representative microscopy images of the colocalization of COX1 and WIPI2 using human healthy and NASH liver tissues. Scale bar = 20 μm. (C) Docking model of COX1 and WIPI2 using I-TASSER software. COX1 and WIPI2 are colored gray and green, respectively. Cartoons, sticks, and surface representations were used to profile the binding mode. (D) The co-IP assay was performed using cell lysates from HEK293T cells co-transfected with GFP-WIPI2 and COX1-FLAG plasmids. COX1 was immunoprecipitated from the transfected HEK293T cells using the FLAG antibody and the eluted proteins were subjected to Western blotting to detect WIPI2-GFP and COX1-FLAG. (E) The co-IP assay was performed using cell lysates from HEK293T cells co-transfected with COX1-HIS and WIPI2-FLAG plasmids. WIPI2 was immunoprecipitated from the transfected HEK293T cells using a FLAG antibody, and the eluted proteins were subjected to Western blotting to detect COX1-HIS and WIPI2-FLAG. (F) The co-IP assay was performed using cell lysates from HEK293T cells co-transfected with COX1-FLAG plasmids. COX1 was immunoprecipitated from the transfected HEK293T cells using a FLAG antibody, and the eluted proteins were subjected to Western blotting to detect COX1-FLAG and endogenous WIPI2. Rabbit IgG antibodies were used as negative controls in the Co-IP assay. Protein lysates (10%) were used as input. IP ratios have been normalized to input ratios to account for differences in input protein levels. (G) Surface plasmon resonance results of the binding of recombinant mouse WIPI2 to immobilized recombinant mouse COX1 protein. A gradient of WIPI2 protein was applied to quantify the binding affinity (62.5−1000 nmol/L). The K_d (mol/L) value is 2.89 × 10^{-6}. (H) The interaction of COX1 with WIPI2 was detected using MST, with 3500 nmol/L as the highest and 100 nmol/L as the lowest COX1 concentration. K_d is 3.95 × 10^{-8} mol/L.

steatosis markers (*Scd1*, *Ppar-γ* and *Cd36*) (Fig. 7B−D; Fig. S9B−S9E). In addition, we observed improved hepatic inflammation as evidenced by a decreased number of F4/80-positive cells and mRNA levels of inflammation markers (*Tnf-α*, *Il-6*, and *Il-1β*) after AAV-mediated rescue of WIPI2 in *Cox1*$^{\Delta hepa}$ mice (Fig. 7B and D). However, there was only a modest decrease in serum AST levels (Fig. S9E), whereas the serum ALT level and the liver to body weight remained unchanged following AAV8-WIPI2 injection in *Cox1*$^{\Delta hepa}$ mice (Fig. S9F−S9H). Overall, these results indicate that hepatic WIPI2 restoration partially rescued the increased steatosis and inflammation in *Cox1*$^{\Delta hepa}$ mice in an autophagy-dependent manner.

3.8. *COX2 was not involved in the protective roles of COX1 in autophagy*

COX2 inhibition has been reported to alleviate hepatocyte senescence in NAFLD[38,39], whereas our work suggests COX1 is unlike COX2 and plays an essential role in the prevention of NAFLD. To clarify the roles of COX1 and COX2 in autophagy and NASH, we first measured both protein and mRNA levels of COX2 in *Cox1*-knockdown AML12 cells and in the livers of *Cox1*$^{\Delta hepa}$ mice. We found that COX2 level was not influenced by COX1 deletion (Supporting Information Fig. S10A−S10D). Second, under NASH condition, COX2 level was significantly higher in *Cox1*$^{\Delta hepa}$ mice compared to their control *Cox1*$^{f/f}$ mice (Fig. S10C and S10D), which is consistent with the fact that *Cox1*$^{\Delta hepa}$ mice exhibited more severe inflammation as indicated by mRNA levels of inflammatory markers *Tnf-α*, *Il-6*, and *Il-1β* (Fig. 4F). Next, we predicted the binding mode between WIPI2 and COX1/COX2 using ZDOCK software (Worcester, MA, USA). We noticed that COX1/COX2 had distinct binding locations for WIPI2, which might have contributed to their various biological activities (Fig. S10E−S10G). According to the per-residue decomposition based on the MM/GBSA method, the binding of WIPI2 to the COX1 primarily contributed to the residues of Lys32, Ser33, Leu75, Arg356, and Asp358 (Fig. S10F), while those for WIPI2 to the COX1 were Val262, Ser264, Gly265, Phe296, and Gln344 (Fig. S10G). However, COX2 did not interact with WIPI2 as did COX1, as shown by the co-IP experiments (Fig. S10H). These results suggest that COX2 may not participate in the impaired autophagy and steatohepatitis caused by *Cox1* deletion.

4. Discussion

A growing body of evidence suggests that impaired autophagy is involved in the pathogenesis of NASH. Unfortunately, the molecular mechanisms underlying autophagic dysfunction in disease progression are poorly understood, and effective therapeutic strategies targeting autophagy are limited. Unlike COX2, which has been extensively explored in the inflammatory response and cancer progression, very little information about the pathophysiological significance of COX1 in liver diseases is available, probably due to the low and constitutive expression nature of COX1 in the liver. Our previous data demonstrated that the basal expression of COX1 was essential for the protection of chemically induced acute liver injury and required for hepatic homeostatic maintenance[10]. In this study, we first found COX1 deficiency impaired autophagic flux in AML12 hepatocytes, and hepatic specific COX1 deletion aggravated steatohepatitis through the inhibition of autophagy in mice NASH models. Further investigations demonstrated that COX1 performed a vital protective function in autophagy through direct interaction with WIPI2. Together, our results suggest that the COX1−WIPI2 axis has a novel protective role in hepatic autophagy function in the pathogenesis of NASH.

Although *Cox1* deletion resulted in impaired autophagic flux both in the liver and in AML12 hepatocytes, *Cox1*$^{\Delta hepa}$ mice did not exhibit any histological differences under chow diet-fed conditions. However, when challenged with a high-fat diet, these mice exhibited severe steatohepatitis. When *Cox1* was knocked down in AML12 cells, we observed significantly increased lipid accumulation. The inconsistent results of lipid accumulation *in vivo* and *in vitro* implied that, while deletion of hepatocyte-COX1 resulted in impaired autophagic flux, this was not enough for obvious lipid accumulation in the liver since other cell types, such as macrophages, may compensate or supplement the loss of COX1 in hepatocytes through unknown mechanisms, for example, exogenous sources of prostaglandins[40].

It is critically important to identify the contributing factors for the development and progression of NASH, which is a multifactorial disease with substantial genetic components. To date, several genome-wide association studies have identified several single-nucleotide polymorphisms associated with this trait, such as *PNPLA3*, *TM6SF2*, and *Klotho*[41−45]. It is noteworthy that several genetic variants were identified in human *COX1*, which altered basal COX1-mediated arachidonic acid metabolism, which is a precursor of proinflammatory compounds[46]. It has been well-recognized that increased levels of AA may cause NASH deterioration[47]. Thus, the functional impact of these variants *in vivo* and whether these genetic variants are associated with NASH progression need to be deeply examined. Considering that our study suggests *Cox1* serves as a protective gene based on increased COX1 expression in the livers of NASH patients, we propose that COX1 genetic variants may predispose patients to aggravated steatohepatitis.

The role of hepatic COX1 and autophagy and their involvement in the disease progression of NASH have not been explored in existing research. We found that *Cox1*$^{\Delta hepa}$ mice exhibited increased LC3II levels but showed no histopathological changes. TEM analysis also revealed more autophagic vacuoles in the livers of *Cox1*$^{\Delta hepa}$ mice. While NASH induction significantly increased LC3II in *Cox1*$^{f/f}$ mice, it failed to induce LC3II expression in *Cox1*$^{\Delta hepa}$ mice. Pharmacological inhibition of autophagy by CQ exacerbated diet-induced liver injury in *Cox1*$^{f/f}$ mice, whereas these effects of CQ were abrogated in *Cox1*$^{\Delta hepa}$ mice. These data suggest that impaired autophagic might be responsible for the exacerbated steatohepatitis in *Cox1*$^{\Delta hepa}$ mice. Notably, CQ treatment did not affect the accumulation of LC3II induced by *Cox1* knockdown in the cell experiments, but it did affect the accumulation of LC3II in the CDAA-treated *Cox1*$^{\Delta hepa}$ group. We infer that the accumulation of LC3II result from a balance of COX1 deletion and CQ treatment under different conditions. For *in vitro* cell experiments, while ablation of COX1 induced an accumulation of LC3II, it failed to cause a further accumulation of LC3II upon late-stage autophagy inhibition with BafA or CQ, suggesting that COX1 deficiency-induced accumulation of LC3II was not a result of increased autophagy onset but autophagy inhibition. However, under NASH conditions, the scenario became much more complicated. The dosage of CQ required to achieve suppression of autophagy with exacerbated hepatic steatosis and liver injury was 60 mg/kg, as reported by other studies[2]. We suspect that the effects of autophagy inhibition

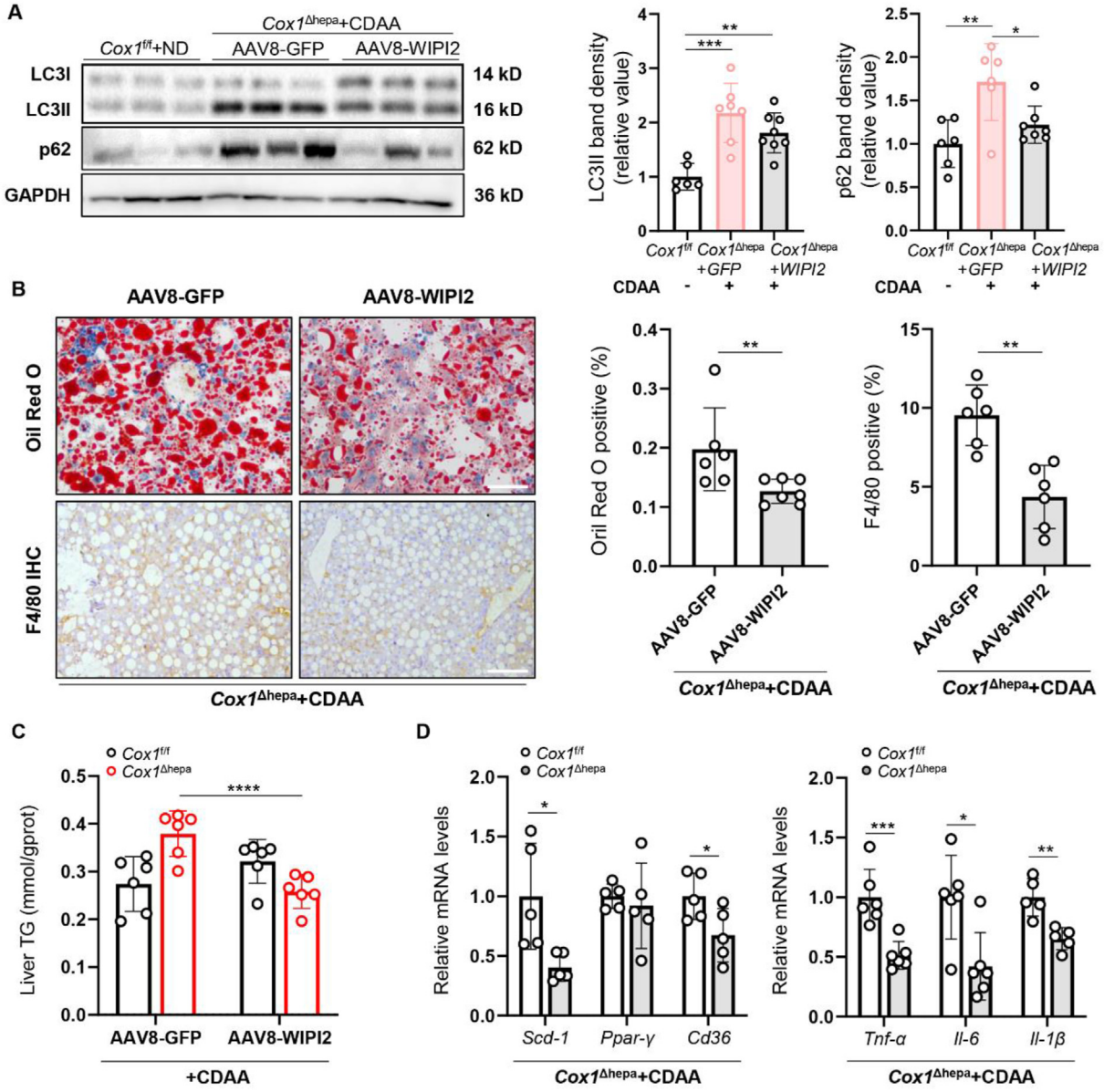

Figure 7 Liver-specific restoration of WIPI2 reduced hepatic lipid accumulation and inflammation in *Cox1*$^{\Delta hepa}$ mice under NASH condition. (A) Western blotting and corresponding quantification of LC3I/II and p62 proteins from the livers of *Cox1*$^{\Delta hepa}$ mice injected with AAV8-GFP or AAV8-WIPI2 viruses (n = 6−8). (B) Representative microscopic images and quantifications of liver sections stained with Oil Red O and F4/80 in *Cox1*$^{\Delta hepa}$ mice injected with the AAV8-GFP or AAV8-WIPI2 viruses (n = 6−7). Scale bar = 10 μm. (C) Hepatic TG levels in *Cox1* $^{f/f}$ and *Cox1*$^{\Delta hepa}$ mice injected with AAV8-GFP or AAV8-WIPI2 viruses (n = 6). (D) mRNA levels of key genes of lipid metabolism (*Scd-1*, *Ppar-γ*, and *Cd36*) and inflammation (*Tnf-α*, *Il-6*, and *Il-1β*) in the livers from *Cox1* $^{f/f}$ and *Cox1*$^{\Delta hepa}$ mice injected with the AAV8-GFP or AAV8-WIPI2 viruses (n = 5−6/group). Values represent means ± SD. Statistical comparisons among groups were analyzed using a one-way ANOVA or Student's t test. *P < 0.05; **P < 0.01; ***P < 0.001; ****P < 0.0001. IHC, immunohistochemistry; CDAA, a choline-deficient, L-amino acid−defined, high-fat diet enriched with 1% cholesterol; TG, triglyceride; Scd1, stearoyl-coA desaturase-1; Ppar-γ, peroxisome proliferator-activated receptor gamma; Tnf-α, necrosis factor α; Il-6, interleukin 6; Il-1β, interleukin 1β. The Western blotting bands of LC3I/II were cut and re-arranged because of the loading order. Original images with detailed labeling information can be found in Supporting Information.

by CQ in this scenario are stronger than the effects of *Cox1* deletion.

PI(3)P, generated by PI3K, is critical for autophagosome formation and autophagosome maturation/autolysosome formation[33,48,49]. Mammalian cells have several PI3Ks, of which class III PI3K has multiple roles in autophagy by forming different complexes[33]. PI(3)P promotes the localization of PI(3)P effector proteins with PI(3)P-binding motifs such as the FYVE domains or through PROPPIN repeats for WIPI2[33]. In our study, we unraveled an unexpected colocalization between COX1 and WIPI2 and not for the DFCP1 or FYVE domains. The direct binding between these 2 proteins was validated following co-IP analyses and *in vitro* biophysical assays. WIPI2 is required for LC3 lipidation, which places WIPI2 at a truly central position in autophagosome

biogenesis[50,51]. While most studies show that WIPI2 is essential for autophagosome formation[50,52], the precise roles of WIPI2 protein and whether it has redundant or independent functions are still under investigation[53]. Although several studies illustrate that phagophore development is suppressed in the absence of WIPI2, LC3 lipidation is partially inhibited or, in some circumstances, unaffected[52,54−56]. Importantly, Wan et al.[56] first demonstrated an unexpectedly high affinity of WIPI2 for PI(4)P by using an *in vitro* lipid-protein overlay experiment. They proposed that WIPI2 on autophagosomes might play a key role in the fusion of autophagosome and lysosomes by acting as a PI(4)P effector, based on the fact that GABA type a receptor-associated protein (GABARAP)-mediated recruitment of PI4KIIa has been shown to produce PI(4)P on autophagosomal membranes, and that autophagosome-located PI(4)P promotes autophagosome −lysosome fusion[57]. Other evidence also showed that some critical autophagic elements could be responsible for both autophagosomes formation and autophagosome maturation in the late stage, including Vps34[58], Atg14 (autophagy-related 14)[48,59] STX17[59,60] and VCP[61,62]. In terms of Vps34 complex, autolysosome was dysfunctional in Vps34-Null MEFs and autophagic flux was blocked in *Vps34*$^{-/-}$ livers, while this complex is essential for the formation of the phagophore through regulating the local synthesis of PI(3)P[62]. Our results support the hypothesis that WIPI2 on autophagosomes may contribute to autolysosome formation; nevertheless, further experimental evidence is required.

The autophagic regulation mechanisms of WIPI2 have been well-studied; however, the understanding of its pathophysiological functions in liver diseases remains limited. Recently, Wan et al.[56] reported that mTORC1-mediated WIPI2 phosphorylation regulated autophagy and consequent lipid clearance in the mouse liver. Nevertheless, this study only evaluated the physiological function of WIPI2. Our study observed a dramatic decrease in WIPI2 expression in the mouse liver of HFHC- and CDAA-induced NASH models (Supporting Information Fig. S11A and S11B). However, AAV-mediated rescue of hepatic WIPI2 failed to rescue NASH-related phenotypes, indicating that increasing WIPI2 alone might not effectively promote the clearance of excess lipid drops under NASH conditions. Importantly, hepatic restoration of WIPI2 partially reversed the hepatic inflammation and steatosis in *Cox1*$^{\Delta hepa}$ mice, indicating that COX1 deletion-mediated impaired autophagic flux was at least partially dependent on WIPI2−mediated autophagy. Considering that COX1 deletion resulted in a marked decrease in WIPI2 protein expression (Fig. S11A), we propose that COX1 mediates its autophagic function through WIPI2, which implies a potential role of the COX1−WIPI2 axis in the pathological process of NASH. Given the numerous structural similarities between COX1 and COX2, we tried to ascertain why COX2 did not interact with WIP2 by determining which domain is responsible for the interaction between COX1 and WIPI2. Both COX isoforms consist of 3 domains: the epidermal growth factor (EGF) domain, the membrane-bound domain (MBD), and the catalytic domain containing the COX active site (the most strongly conserved region in COX isoforms)[63]. We suspect that the EGF-like domain and MBD are where WIPI2 and COXs interact differentially. This is supported by the fact that the EGF-like domain is frequently found in integral membrane proteins, and the MBD contains a number of amino acids that allow COXs to interact with the lipid bilayer[64,65]. Unfortunately, since WIPI2 was shown to bind all of the various COX1 truncated proteins, we were thus unable to determine which COX1 domain is responsible for WIPI2 binding (Supporting Information Fig. S12). Although this may indicate that WIPI2 can interact with COX1 at several sites, this could also be a consequence of improper folding of the COX1 truncations. Nevertheless, this point should be further examined in future studies.

Ferroptosis is characterized by the formation of reactive oxygen species from iron accumulation and lipid peroxidation, which is a novel form of regulated cell death[66]. Based on the original study from Dr. Stockwell in 2012, ferroptosis induced by erastin in cancer cells results in the loss of the morphological and biochemical characteristics of apoptosis, necrosis, and autophagy[67]. While potent autophagy inhibitors (*e.g.*, BafA, 3-methyladenine, and CQ) failed to prevent erastin-induced ferroptosis in certain cancer cells[67], genetic inhibition of the autophagic pathway by knockout or knockdown of Atg5, Atg7, Atg16L1 and nuclear receptor coactivator 4 ameliorated erastin-induced ferroptosis with decreased intracellular ferrous iron levels, and lipid peroxidation[54,68]. These findings provide novel insight into the ferroptosis as an autophagic cell death process. However, these investigations were conducted mostly in cancer cells and immortalized mouse embryonic fibroblasts. With respect to liver diseases, ferroptosis has been recently found to be implicated in liver disease[69−71] including NAFLD[69,72,73]. Several seminal studies reported the therapeutic effects of iron chelators and ferroptosis inhibitors may prevent metabolic syndrome and steatohepatitis in experimental fatty liver mice models[72,74,75]. Moreover, knockout of iron chaperones of the poly(rC) binding protein 1 was shown to disrupt liver iron homeostasis, resulting in steatosis and inflammation in mice[76]. Ferroptosis is a form of inflammatory cell death associated with increased COX2 expression and the release of PGE2 during tissue injury[77,78], and ferroptosis inhibitors have demonstrated benefits due to their anti-inflammatory activity in certain diseases, which appears to be linked to inflammation through eicosanoid synthesis by controlling the activities of lipoxygenases and COXs[79,80]. For example, PGE2 was recently reported to be positively correlated with ferroptosis, and inhibited ferroptosis induced by cerebral ischemia−reperfusion, possibly *via* PGE2 receptor 3 and PGE2 receptor 4[81]. However, little research has been conducted on the role of COX1 in ferroptosis in terms of autophagic cell death process. Considering that COX1 was necessary for functional autophagic flux against steatohepatitis, and that ferroptosis might be implicated in steatohepatitis as an autophagic cell death process associated with iron accumulation and lipid peroxidation, we would propose that COX1 may have a function in autophagic degradation of cellular iron storage proteins (a process known as ferritinophagy) in ferroptosis, which needs to be confirmed in further investigations.

5. Conclusions

Our data suggest that hepatic COX1 is crucial for autophagic function *via* its interaction with WIPI2. Therefore, this study has identified a previously unknown role of the COX1−WIPI2 axis in protecting against NASH by maintaining basal levels of hepatic autophagy.

Acknowledgments

This work was partly supported by National Natural Science Foundation of China (82125026 and 82122009), Natural Science

Foundation of Shandong Province (ZR2022QH241 and ZR2020ZD11, China) and Seed Fund for Basic Research of University Research Committee of The University of Hong Kong (20161159263, Hong Kong, China).

Author contributions

Conceptualization: Qian Yu, Chang Li, George L. Tipoe and Jia Xiao; Methodology and Investigation: Qian Yu, Chang Li, Qinghui Niu, Zhaodi Che, Ke Lei, Zhaodi Che, Zhaohui Liu, Yixing Ren, Pingping Luo and Huan Zhang; Validation: Jigang Wang, Zhuming Fan and Boyi Ma; Formal analysis: Qian Yu and Chang Li; Resources: He Ren, George L. Tipoe and Jia Xiao. Data Curation: Qian Yu and Chang Li; Writing-Original Draft: Qian Yu and Chang Li; Writing-Review and Editing: George L. Tipoe and Jia Xiao; Visualization: Qian Yu, Zhuming Fan and Jia Xiao; Supervision: He Ren, George L. Tipoe and Jia Xiao; Project administration: Qian Yu and Chang Li; Funding acquisition: Qian Yu, He Ren, George L. Tipoe and Jia Xiao.

Conflicts of interest

The authors declare no conflicts of interest.

Appendix A. Supporting information

Supporting data to this article can be found online at https://doi.org/10.1016/j.apsb.2023.03.008.

References

1. Vernon G, Baranova A, Younossi ZM. Systematic review: the epidemiology and natural history of non-alcoholic fatty liver disease and non-alcoholic steatohepatitis in adults. *Aliment Pharmacol Ther* 2011;**34**:274−85.
2. Lin CW, Zhang H, Li M, Xiong X, Chen X, Chen X, et al. Pharmacological promotion of autophagy alleviates steatosis and injury in alcoholic and non-alcoholic fatty liver conditions in mice. *J Hepatol* 2013;**58**:993−9.
3. Alkhouri N. NASH and NAFLD: emerging drugs, therapeutic targets and translational and clinical challenges. *Expert Opin Investig Drugs* 2020;**29**:87.
4. Polyzos SA, Kountouras J, Mantzoros CS. Obesity and nonalcoholic fatty liver disease: from pathophysiology to therapeutics. *Metabolism* 2019;**92**:82−97.
5. Khambu B, Yan S, Huda N, Liu G, Yin XM. Autophagy in non-alcoholic fatty liver disease and alcoholic liver disease. *Liver Res* 2018;**2**:112−9.
6. Kirschke H, Langner J, Wiederanders B, Ansorge S, Bohley P, Cathepsin L. A new proteinase from rat-liver lysosomes. *Eur J Biochem* 1977;**74**:293−301.
7. Kim YS, Nam HJ, Han CY, Joo MS, Jang K, Jun DW, et al. Liver X receptor alpha activation inhibits autophagy and lipophagy in hepatocytes by dysregulating autophagy-related 4B cysteine peptidase and Rab-8B, reducing mitochondrial fuel oxidation. *Hepatology* 2021;**73**:1307−26.
8. Wang D, Dubois RN. Prostaglandins and cancer. *Gut* 2006;**55**:115−22.
9. Daikoku T, Wang D, Tranguch S, Morrow JD, Orsulic S, DuBois RN, et al. Cyclooxygenase-1 is a potential target for prevention and treatment of ovarian epithelial cancer. *Cancer Res* 2005;**65**:3735−44.
10. Xiao J, Liong EC, Huang H, On Tse W, Lau KS, Pan J, et al. Cyclooxygenase-1 serves a vital hepato-protective function in chemically induced acute liver injury. *Toxicol Sci* 2015;**143**:430−40.
11. Lim JS, Mietus-Snyder M, Valente A, Schwarz JM, Lustig RH. The role of fructose in the pathogenesis of NAFLD and the metabolic syndrome. *Nat Rev Gastroenterol Hepatol* 2010;**7**:251−64.
12. Tølbøl KS, Stierstorfer B, Rippmann JF, Veidal SS, Rigbolt KTG, Schönberger T, et al. Disease progression and pharmacological intervention in a nutrient-deficient rat model of nonalcoholic steatohepatitis. *Dig Dis Sci* 2019;**64**:1238−56.
13. Caballero F, Fernández A, Matías N, Martínez L, Fucho R, Elena M, et al. Specific contribution of methionine and choline in nutritional nonalcoholic steatohepatitis: impact on mitochondrial *S*-adenosyl-L-methionine and glutathione. *J Biol Chem* 2010;**285**:18528−36.
14. Gao H, Lv Y, Liu Y, Li J, Wang X, Zhou Z, et al. Wolfberry-derived zeaxanthin dipalmitate attenuates ethanol-induced hepatic damage. *Mol Nutr Food Res* 2019;**63**:e1801339.
15. Berleth M, Berleth N, Minges A, Hänsch S, Burkart RC, Stork B, et al. Molecular analysis of protein−protein interactions in the ethylene pathway in the different ethylene receptor subfamilies. *Front Plant Sci* 2019;**10**:726.
16. Roy A, Kucukural A, Zhang Y. I-TASSER: a unified platform for automated protein structure and function prediction. *Nat Protoc* 2010;**5**:725−38.
17. Xu JR, Zhang Y. How significant is a protein structure similarity with TM-score = 0.5?. *Bioinformatics* 2010;**26**:889−95.
18. Yan Y, Zhang D, Zhou P, Li B, Huang SY. HDOCK: a web server for protein−protein and protein−DNA/RNA docking based on a hybrid strategy. *Nucleic acids Res* 2017;**45**:W365−73.
19. Case DA, Cheatham TE, Darden T, Gohlke H, Luo R, Merz KM, et al. The amber biomolecular simulation programs. *J Comput Chem* 2005;**26**:1668−88.
20. Maier JA, Martinez C, Kasavajhala K, Wickstrom L, Hauser KE, Simmerling C. ff14SB: improving the accuracy of protein side chain and backbone parameters from ff99SB. *J Chem Theory Comput* 2015;**11**:3696−713.
21. Gohlke H, Case DA. Converging free energy estimates: MM-PB(GB)SA studies on the protein−protein complex Ras−Raf. *J Comput Chem* 2004;**25**:238−50.
22. Onufriev A, Bashford D, Case DA. Exploring protein native states and large-scale conformational changes with a modified generalized born model. *Proteins* 2004;**55**:383−94.
23. Tian C, Kasavajhala K, Belfon KAA, Raguette L, Huang H, Migues AN, et al. ff19SB: amino-acid-specific protein backbone parameters trained against quantum mechanics energy surfaces in solution. *J Chem Theory Comput* 2020;**16**:528−52.
24. Darden T, York D, Pedersen L. Particle mesh Ewald: an N•log(N) method for Ewald sums in large systems. *J Chem Phys* 1993;**98**:10089−92.
25. Ryckaert JP, Ciccotti G, Berendsen HJC. Numerical integration of the cartesian equations of motion of a system with constraints: molecular dynamics of *n*-alkanes. *J Chem Phys* 1977;**23**:327−41.
26. Roe DR, Cheatham 3rd TE. PTRAJ and CPPTRAJ: software for processing and analysis of molecular dynamics trajectory data. *J Chem Theory Comput* 2013;**9**:3084−95.
27. Grant BJ, Rodrigues AP, ElSawy KM, McCammon JA, Caves LS. Bio3d: an R package for the comparative analysis of protein structures. *Bioinformatics* 2006;**22**:2695−6.
28. Humphrey W, Dalke A, Schulten K. VMD: visual molecular dynamics. *J Mol Graph* 1996;**14**:27−8.
29. Jaber N, Dou Z, Chen JS, Catanzaro J, Jiang YP, Ballou LM, et al. Class III PI3K Vps34 plays an essential role in autophagy and in heart and liver function. *Proc Natl Acad Sci U S A* 2012;**109**:2003−8.
30. Kundu ST, Grzeskowiak CL, Fradette JJ, Gibson LA, Rodriguez LB, Creighton CJ, et al. TMEM106B drives lung cancer metastasis by inducing TFEB-dependent lysosome synthesis and secretion of cathepsins. *Nat Commun* 2018;**9**:2731.
31. Zhao YG, Codogno P, Zhang H. Machinery, regulation and pathophysiological implications of autophagosome maturation. *Nat Rev Mol Cell Biol* 2021;**22**:733−50.

32. Jean S, Cox S, Nassari S, Kiger AA. Starvation-induced MTMR13 and RAB21 activity regulates VAMP8 to promote autophagosome−lysosome fusion. *EMBO Rep* 2015;**16**:297−311.
33. Kawabata T, Yoshimori T. Autophagosome biogenesis and human health. *Cell Discov* 2020;**6**:33.
34. Nascimbeni AC, Codogno P, Morel E. Phosphatidylinositol-3-phosphate in the regulation of autophagy membrane dynamics. *FEBS J* 2017;**284**:1267−78.
35. Vicinanza M, Korolchuk VI, Ashkenazi A, Puri C, Menzies FM, Clarke JH, et al. PI(5)P regulates autophagosome biogenesis. *Mol Cell* 2015;**57**:219−34.
36. Douzi B. Protein−protein interactions: surface plasmon resonance. *Methods Mol Biol* 2017;**1615**:257−75.
37. Sparks RP, Fratti R. Use of microscale thermophoresis (MST) to measure binding affinities of components of the fusion machinery. *Methods Mol Biol* 2019;**1860**:191−8.
38. Liu C, Liu L, Zhu HD, Sheng JQ, Wu XL, He XX, et al. Celecoxib alleviates nonalcoholic fatty liver disease by restoring autophagic flux. *Sci Rep* 2018;**8**:4108.
39. Zhang CY, Tan XH, Yang HH, Jin L, Hong JR, Zhou Y, et al. COX-2/sEH dual inhibitor alleviates hepatocyte senescence in NAFLD mice by restoring autophagy through Sirt1/PI3K/AKT/mTOR. *Int J Mol Sci* 2022;**23**:8267.
40. Omura N, Griffith M, Vincent A, Li A, Hong SM, Walter K, et al. Cyclooxygenase-deficient pancreatic cancer cells use exogenous sources of prostaglandins. *Mol Cancer Res* 2010;**8**:821−32.
41. Dongiovanni P, Crudele A, Panera N, Romito I, Meroni M, De Stefanis C, et al. β-Klotho gene variation is associated with liver damage in children with NAFLD. *J Hepatol* 2020;**72**:411−9.
42. Dongiovanni P, Petta S, Maglio C, Fracanzani AL, Pipitone R, Mozzi E, et al. Transmembrane 6 superfamily member 2 gene variant disentangles nonalcoholic steatohepatitis from cardiovascular disease. *Hepatology* 2015;**61**:506−14.
43. Kozlitina J, Smagris E, Stender S, Nordestgaard BG, Zhou HH, Tybjærg-Hansen A, et al. Exome-wide association study identifies a TM6SF2 variant that confers susceptibility to nonalcoholic fatty liver disease. *Nat Genet* 2014;**46**:352−6.
44. Romeo S, Kozlitina J, Xing C, Pertsemlidis A, Cox D, Pennacchio LA, et al. Genetic variation in PNPLA3 confers susceptibility to nonalcoholic fatty liver disease. *Nat Genet* 2008;**40**:1461−5.
45. Valenti L, Alisi A, Galmozzi E, Bartuli A, Del Menico B, Alterio A, et al. I148M patatin-like phospholipase domain-containing 3 gene variant and severity of pediatric nonalcoholic fatty liver disease. *Hepatology* 2010;**52**:1274−80.
46. Lee CR, Bottone Jr FG, Krahn JM, Li L, Mohrenweiser HW, Cook ME, et al. Identification and functional characterization of polymorphisms in human cyclooxygenase-1 (PTGS1). *Pharmacogenet Genom* 2007;**17**:145−60.
47. Patterson E, Wall R, Fitzgerald GF, Ross RP, Stanton C. Health implications of high dietary omega-6 polyunsaturated Fatty acids. *J Nutr Metab* 2012;**2012**:539426.
48. Diao J, Liu R, Rong Y, Zhao M, Zhang J, Lai Y, et al. ATG14 promotes membrane tethering and fusion of autophagosomes to endolysosomes. *Nature* 2015;**520**:563−6.
49. Matsunaga K, Saitoh T, Tabata K, Omori H, Satoh T, Kurotori N, et al. Two Beclin 1-binding proteins, Atg14L and Rubicon, reciprocally regulate autophagy at different stages. *Nat Cell Biol* 2009;**11**:385−96.
50. Dooley HC, Razi M, Polson HE, Girardin SE, Wilson MI, Tooze SA. WIPI2 links LC3 conjugation with PI3P, autophagosome formation, and pathogen clearance by recruiting Atg12-5-16L1. *Mol Cell* 2014;**55**:238−52.
51. Fracchiolla D, Chang C, Hurley JH, Martens S. A PI3K-WIPI2 positive feedback loop allosterically activates LC3 lipidation in autophagy. *J Cell Biol* 2020;**219**:e201912098.
52. Polson HE, de Lartigue J, Rigden DJ, Reedijk M, Urbé S, Clague MJ, et al. Mammalian Atg18 (WIPI2) localizes to omegasome-anchored phagophores and positively regulates LC3 lipidation. *Autophagy* 2010;**6**:506−22.
53. Dudley LJ, Makar AN, Gammoh N. Membrane targeting of core autophagy players during autophagosome biogenesis. *FEBS J* 2020;**287**:4806−21.
54. Dudley LJ, Cabodevilla AG, Makar AN, Sztacho M, Michelberger T, Marsh JA, et al. Intrinsic lipid binding activity of ATG16L1 supports efficient membrane anchoring and autophagy. *EMBO J* 2019;**38**:e100554.
55. Lystad AH, Carlsson SR, de la Ballina LR, Kauffman KJ, Nag S, Yoshimori T, et al. Distinct functions of ATG16L1 isoforms in membrane binding and LC3B lipidation in autophagy-related processes. *Nat Cell Biol* 2019;**21**:372−83.
56. Wan W, You Z, Zhou L, Xu Y, Peng C, Zhou T, et al. mTORC1-regulated and HUWE1-mediated WIPI2 degradation controls autophagy flux. *Mol Cell* 2018;**72**:303−15. e6.
57. Wang H, Sun HQ, Zhu X, Zhang L, Albanesi J, Levine B, et al. GABARAPs regulate PI4P-dependent autophagosome:lysosome fusion. *Proc Natl Acad Sci U S A* 2015;**112**:7015−20.
58. Backer JM. The regulation and function of class III PI3Ks: novel roles for Vps34. *Biochem J* 2008;**410**:1−17.
59. Hamasaki M, Furuta N, Matsuda A, Nezu A, Yamamoto A, Fujita N, et al. Autophagosomes form at ER-mitochondria contact sites. *Nature* 2013;**495**:389−93.
60. Itakura E, Kishi-Itakura C, Mizushima N. The hairpin-type tail-anchored SNARE syntaxin 17 targets to autophagosomes for fusion with endosomes/lysosomes. *Cell* 2012;**151**:1256−69.
61. Hill SM, Wrobel L, Ashkenazi A, Fernandez-Estevez M, Tan K, Bürli RW, et al. VCP/p97 regulates Beclin-1-dependent autophagy initiation. *Nat Chem Biol* 2021;**17**:448−55.
62. Tresse E, Salomons FA, Vesa J, Bott LC, Kimonis V, Yao TP, et al. VCP/p97 is essential for maturation of ubiquitin-containing autophagosomes and this function is impaired by mutations that cause IBMPFD. *Autophagy* 2010;**6**:217−27.
63. Kim SF. The nitric oxide-mediated regulation of prostaglandin signaling in medicine. *Vitam Horm* 2014;**96**:211−45.
64. Garavito RM, Malkowski MG, DeWitt DL. The structures of prostaglandin endoperoxide H synthases-1 and -2. *Prostaglandins Other Lipid Mediat* 2002;**68**−**69**:129−52.
65. MirAfzali Z, Leipprandt JR, McCracken JL, DeWitt DL. Topography of the prostaglandin endoperoxide H2 synthase-2 in membranes. *J Biol Chem* 2006;**281**:28354−64.
66. Xie Y, Hou W, Song X, Yu Y, Huang J, Sun X, et al. Ferroptosis: process and function. *Cell Death Differ* 2016;**23**:369−79.
67. Dixon SJ, Lemberg KM, Lamprecht MR, Skouta R, Zaitsev EM, Gleason CE, et al. Ferroptosis: an iron-dependent form of non-apoptotic cell death. *Cell* 2012;**149**:1060−72.
68. Hou W, Xie Y, Song X, Sun X, Lotze MT, Zeh 3rd HJ, et al. Autophagy promotes ferroptosis by degradation of ferritin. *Autophagy* 2016;**12**:1425−8.
69. Li L, Wang K, Jia R, xie J, Ma L, Hao Z, et al. Ferroportin-dependent ferroptosis induced by ellagic acid retards liver fibrosis by impairing the SNARE complexes formation. *Redox Biol* 2022;**56**:102435.
70. Chen J, Li X, Ge C, Min J, Wang F. The multifaceted role of -ferroptosis in liver disease. *Cell Death Differ* 2022;**29**:467−80.
71. Wu Y, Jiao H, Yue Y, He K, Jin Y, Zhang J, et al. Ubiquitin ligase E3 HUWE1/MULE targets transferrin receptor for degradation and suppresses ferroptosis in acute liver injury. *Cell Death Differ* 2022;**29**:1705−18.
72. Tong J, Lan XT, Zhang Z, Liu Y, Sun DY, Wang XJ, et al. Ferroptosis inhibitor liproxstatin-1 alleviates metabolic dysfunction-associated fatty liver disease in mice: potential involvement of PANoptosis. *Acta Pharmacol Sin* 2023;**44**:1014−28.
73. Tong J, Li D, Meng H, Sun D, Lan X, Ni M, et al. Targeting a novel inducible GPX4 alternative isoform to alleviate ferroptosis and treat metabolic-associated fatty liver disease. *Acta Pharm Sin B* 2022;**12**:3650−66.

74. Qi J, Kim JW, Zhou Z, Lim CW, Kim B. Ferroptosis affects the progression of nonalcoholic steatohepatitis *via* the modulation of lipid peroxidation-mediated cell death in mice. *Am J Pathol* 2020;**190**:68−81.
75. Li X, Wang TX, Huang X, Li Y, Sun T, Zang S, et al. Targeting ferroptosis alleviates methionine-choline deficient (MCD)-diet induced NASH by suppressing liver lipotoxicity. *Liver Int* 2020;**40**:1378−94.
76. Protchenko O, Baratz E, Jadhav S, Li F, Shakoury-Elizeh M, Gavrilova O, et al. Iron chaperone poly rC binding protein 1 protects mouse liver from lipid peroxidation and steatosis. *Hepatology* 2021;**73**:1176−93.
77. Tang D, Chen X, Kang R, Kroemer G. Ferroptosis: molecular mechanisms and health implications. *Cell Res* 2021;**31**:107−25.
78. Yang WS, SriRamaratnam R, Welsch ME, Shimada K, Skouta R, Viswanathan VS, et al. Regulation of ferroptotic cancer cell death by GPX4. *Cell* 2014;**156**:317−31.
79. Song Y, Wu Z, Xue H, Zhao P. Ferroptosis is involved in regulating perioperative neurocognitive disorders: emerging perspectives. *J Neuroinflammation* 2022;**19**:219.
80. Schneider M, Wortmann M, Mandal PK, Arpornchayanon W, Jannasch K, Alves F, et al. Absence of glutathione peroxidase 4 affects tumor angiogenesis through increased 12/15-lipoxygenase activity. *Neoplasia* 2010;**12**:254−63.
81. Xu Y, Liu Y, Li K, Yuan D, Yang S, Zhou L, et al. COX-2/PGE2 pathway inhibits the ferroptosis induced by cerebral ischemia reperfusion. *Mol Neurobiol* 2022;**59**:1619−31.